

The ALPINE-ALMA [C II] survey: Molecular gas budget in the Early Universe as traced by [C II]

M. Dessauges-Zavadsky¹, M. Ginolfi¹, F. Pozzi^{2,3}, M. Béthermin⁴, O. Le Fèvre⁴, S. Fujimoto^{5,6}, J. D. Silverman^{7,8}, G. C. Jones^{9,10}, D. Schaerer¹, A. L. Faisst¹¹, Y. Khusanova^{4,12}, Y. Fudamoto¹, P. Cassata^{13,14}, F. Loiacono^{2,3}, P. L. Capak^{11,5,6}, L. Yan¹⁵, R. Amorin^{16,17}, S. Bardelli³, M. Boquien¹⁸, A. Cimatti^{2,19}, C. Gruppioni³, N. P. Hathi²⁰, E. Ibar²¹, A. M. Koekemoer²⁰, B. C. Lemaux²², D. Narayanan²³, P. A. Oesch^{1,5}, G. Rodighiero^{13,14}, M. Romano^{13,14}, M. Talia^{2,3}, S. Toft^{6,5}, L. Vallini²⁴, D. Vergani³, G. Zamorani³, and E. Zucca³

(Affiliations can be found after the references)

Received; accepted

ABSTRACT

The molecular gas content of normal galaxies at $z > 4$ is poorly constrained, because the commonly used molecular gas tracers become hard to detect at these redshifts. We use the [C II] 158 μm luminosity, recently proposed as a molecular gas tracer, to estimate the molecular gas content in a large sample of main-sequence star-forming galaxies at $z = 4.4 - 5.9$, with a median stellar mass of $10^{9.7} M_{\odot}$, drawn from the *ALMA Large Program to INvestigate [C II] at Early times* (ALPINE) survey. The good agreement between molecular gas masses derived from [C II] luminosities, dynamical masses, and rest-frame 850 μm luminosities, extrapolated from the rest-frame 158 μm continuum, supports [C II] as a reliable tracer of molecular gas in our sample. We find a continuous decline of the molecular gas depletion timescale from $z = 0$ to $z = 5.9$, which reaches a mean value of $(4.6 \pm 0.8) \times 10^8$ yr at $z \sim 5.5$, only a factor of 2 – 3 shorter than in present-day galaxies. This suggests a mild enhancement of star formation efficiency toward high redshifts, unless the molecular gas fraction significantly increases. Our estimates show that the rise in molecular gas fraction as reported previously, flattens off above $z \sim 3.7$ to achieve a mean value of $63\% \pm 3\%$ over $z = 4.4 - 5.9$. This redshift evolution of the gas fraction is in line with the one of the specific star formation rate. We use multi-epoch abundance matching to follow the gas fraction evolution over cosmic time of progenitors of $z = 0$ Milky Way-like galaxies in $\sim 10^{13} M_{\odot}$ halos and of more massive $z = 0$ galaxies in $\sim 10^{14} M_{\odot}$ halos. Interestingly, the former progenitors show a monotonic decrease of the gas fraction with cosmic time, while the latter show a constant gas fraction from $z = 5.9$ to $z \sim 2$ and a steep decrease at $z \lesssim 2$. We discuss three possible effects, namely outflows, halt of gas supplying, and over-efficient star formation, which may jointly contribute to the gas fraction plateau of the latter massive galaxies.

Key words. galaxies: evolution – galaxies: high-redshift – galaxies: ISM – ISM: molecules

1. Introduction

Since cold molecular hydrogen, H_2 , is the fuel for star formation, it is necessary to probe the molecular gas content of galaxies with cosmic time to understand their stellar assembly. With an increasing number of normal star-forming galaxies (SFGs) having measurements of their cold molecular gas mass (M_{molgas}), we are starting to bring to light the significant role that molecular gas plays in the evolution of these galaxies, which contribute to about 90% of the cosmic star formation rate (SFR) density. They are found to follow the star-forming main-sequence (MS), a tight relation between stellar mass (M_{stars}) and SFR, which evolves with redshift and has a dispersion of about ± 0.3 dex (e.g., Rodighiero et al. 2011; Speagle et al. 2014; Whitaker et al. 2014; Tasca et al. 2015; Faisst et al. 2016). The redshift evolution of the MS is such that, at a given M_{stars} , high-redshift galaxies form more stars per unit time than low-redshift galaxies, resulting in an increase of their specific star formation rate ($\text{sSFR} = \text{SFR}/M_{\text{stars}}$) with redshift. It is now well established that, up to $z \sim 2.5$, the sSFR increase is linked to the observed rise of the molecular gas content of galaxies with redshift (e.g., Saintonge et al. 2013; Genzel et al. 2015; Dessauges-Zavadsky et al. 2017; Tacconi et al. 2018, 2020; Decarli et al. 2019). Likewise, the location of a galaxy in the $\text{SFR}-M_{\text{stars}}$ plane is primarily governed by its supply (mass) of molecular gas and to some extent also its star formation efficiency ($\text{SFE} = \text{SFR}/M_{\text{molgas}}$) (e.g.,

Magdis et al. 2012; Dessauges-Zavadsky et al. 2015; Genzel et al. 2015; Silverman et al. 2015, 2018; Scoville et al. 2016; Tacconi et al. 2020).

To explain the high SFR and M_{molgas} of SFGs in the early Universe, it has been proposed that they must be sustained with cold gas accreted from the cosmic web (e.g., Kereš et al. 2005; Dekel et al. 2009). In this context, the MS may be interpreted in terms of a “bathtub” model, in which MS galaxies lie in a quasi-steady state equilibrium whereby star formation is regulated by the available gas reservoir, and whose content is replenished through pristine gas accretion flows and, eventually, diminished by the amount of material galaxies returned to the intergalactic medium through outflows (e.g., Bouché et al. 2010; Davé et al. 2011, 2012; Lilly et al. 2013; Dekel & Mandelker 2014). Beside the average growth of SFGs along the MS, simulations suggest SFGs oscillate up and down in sSFR across the MS dispersion, owing to feedback effects altering the gas accretion rates, internal gas transport, and compaction events (Tacchella et al. 2016; Orr et al. 2019). The bathtub model agrees with most of the scaling relations observed for MS SFGs, such as the Kennicutt-Schmidt star-formation law (Kennicutt 1998b; Tacconi et al. 2013) and the mass-metallicity relation (e.g., Erb et al. 2006; Maiolino et al. 2008; Mannucci et al. 2010; Ginolfi et al. 2019), and with the dynamically more turbulent galactic disks at high-redshift (e.g., Förster Schreiber et al. 2009; Wisnioski et al. 2015; Molina et al. 2017; Girard et al. 2018).

While H_2 is the most abundant molecule in the Universe, it is nevertheless difficult to detect in cold media, because it features no emission lines with excitation temperatures below 100 K. Fortunately, cold molecular gas is not pure H_2 , but contains heavier elements like carbon and oxygen, and is mixed with dust grains. Thus, three indirect cold H_2 tracers are commonly used to estimate the H_2 content of high-redshift galaxies: the CO molecule rotational transitions (Bolatto et al. 2013, and references therein); the dust mass inferred from the fit of the thermal far-infrared (FIR) dust spectral energy distribution (SED) (e.g., Leroy et al. 2011; Magdis et al. 2011; Santini et al. 2014; Béthermin et al. 2015; Kaasinen et al. 2019); and the cold dust continuum emission measured in the Rayleigh-Jeans tail regime of the FIR SED (e.g., Scoville et al. 2014, 2016, 2017). The Plateau de Bure interferometer – now the Northern Extended Millimeter Array (NOEMA) – and the Atacama Large Millimeter/submillimeter Array (ALMA) have largely contributed to the census of M_{molgas} in MS SFGs over the peak of the cosmic star formation from $z = 0$ to $z \sim 3.5$ (e.g., Daddi et al. 2010; Magnelli et al. 2012; Tacconi et al. 2013, 2018; Saintonge et al. 2013, 2017; Santini et al. 2014; Dessauges-Zavadsky et al. 2015; Schinnerer et al. 2016; Decarli et al. 2019; Liu et al. 2019b). At higher redshifts, both CO and dust become harder to detect, because of (i) the surface brightness dimming as $(1+z)^4$, (ii) the lower metallicities expected in distant galaxies making CO dark and dust rare, and (iii) the ALMA bands only covering high ($J \geq 5$) CO transitions at $z > 4.5$, which requires the knowledge of the CO excitation state and gas density to determine the total M_{molgas} . Therefore, only two M_{molgas} estimates derived from CO luminosity measurements were reported in MS SFGs at $z > 5.5$ to date (D’Odorico et al. 2018; Pavesi et al. 2019). And the dozens of M_{molgas} measurements derived from FIR dust continuum for MS SFGs at $z > 4$ (Scoville et al. 2016; Liu et al. 2019b) are largely biased toward massive galaxies with $M_{\text{stars}} \gtrsim 10^{11.5} M_{\odot}$ (and hence high SFRs).

Clearly, the MS is not yet adequately covered at these high redshifts (see the right panel of Fig. 4 of Liu et al. 2019b): molecular gas masses of MS SFGs at $z > 4$, for a large parameter space of M_{stars} and SFR, still need to be accessed to establish how gas reservoirs and gas consumption timescales change as a function of at least three fundamental parameters, namely the cosmic time, M_{stars} , and SFR. The study of the molecular gas content of galaxies over $4 < z < 6$ is all the more important as such redshift range corresponds to the key evolutionary phase in the early life of galaxies, between their primordial and mature phase, with many fundamental properties of present-day galaxies being established (Ribeiro et al. 2016; Feldmann 2015). During this early phase, galaxies are known to double their M_{stars} at 5 to 10 times higher rates than at later cosmic times (Faisst et al. 2016; Davidzon et al. 2018), which may require very efficient star formation and/or considerable supply of molecular gas.

The C^+ radiation, considered as an important coolant of the neutral interstellar medium (ISM), accessible through the [C II] line at $158 \mu\text{m}$ (one of the strongest line in the FIR spectra; see Carilli & Walter 2013) and shown to correlate with the total SFR in galaxies (e.g., De Looze et al. 2011, 2014; Schaerer et al. 2020), has been found to be a good tracer of molecular gas, first at $0.03 < z < 0.2$ by Hughes et al. (2017a) and recently over $0 < z < 6$ by Zanella et al. (2018). Such a correlation between [C II] luminosity (L_{CII}) and M_{molgas} can be exploited to overcome the observational challenge of detecting CO or FIR dust emission in very high-redshift normal SFGs. In this context, our recently completed ALMA Large Program to INvestigate [C II] at Early times (ALPINE; Le Fèvre et al.

2020; Béthermin et al. 2020; Faisst et al. 2020) delivers the first sample of 75 [C II] emission detections and 43 upper limits obtained for a representative population of ultraviolet (UV) selected MS SFGs at $z = 4.4 - 5.9$ with $\text{SFR} \gtrsim 10 M_{\odot} \text{ yr}^{-1}$ and $M_{\text{stars}} = 10^{8.4} - 10^{11} M_{\odot}$. Relying on the Zanella et al. (2018) correlation, we use the ALPINE data to provide the first set of molecular gas mass estimates for MS SFGs at $z = 4.4 - 5.9$.

In Sect. 2 we summarise the ALPINE survey, the physical properties of galaxies in our survey, and the ALMA observations. Measurements of molecular gas masses obtained using [C II] luminosity are presented in Sect. 3, together with specific tests of [C II] as a reliable molecular gas tracer for the ALPINE galaxies. In Sect. 4 we describe the comparison sample, which includes lower redshift MS SFGs with molecular gas masses determined from CO luminosities. We argue why CO-detected MS galaxies represent a better comparison sample with respect to FIR continuum-detected SFGs having typically large M_{stars} . In Sect. 5 we discuss the inferred molecular gas depletion timescales and the molecular gas fractions, which we compare to those of lower redshift CO-detected galaxies. The evolution of the molecular gas fraction over cosmic time is described in Sect. 5.3. We use the multi-epoch abundance matching predictions to connect the progenitors at high redshifts with their descendants at $z = 0$. Our main results are summarised in Sect. 6.

Throughout the paper, we assume the Λ CDM cosmology with $\Omega_m = 0.3$, $\Omega_{\Lambda} = 0.7$ and $H_0 = 70 \text{ km s}^{-1} \text{ Mpc}^{-1}$, and we adopt the Chabrier (2003) initial mass function.

2. Observations and physical properties of ALPINE galaxies

The 118 targeted galaxies from the ALPINE survey (Le Fèvre et al. 2020 – survey paper; Béthermin et al. 2020 – data reduction paper; Faisst et al. 2020 – ancillary data paper) are UV-selected galaxies from the COSMic eVolution Survey (COSMOS, 105 galaxies; Scoville et al. 2007) and the Extended Chandra Deep Field South survey (ECDFS, 13 galaxies; Giacconi et al. 2002). All galaxies have optical spectroscopy, ensuring reliable rest-frame UV spectroscopic redshift measurements, and benefit from multi-wavelength ground- and space-based imaging from UV to IR.

The detailed description of the ancillary spectra and photometric data can be found in Faisst et al. (2020), together with the redshift measurements and the SED fits. The derived M_{stars} and SFR of ALPINE galaxies are in the range of $M_{\text{stars}} = 10^{8.4} - 10^{11} M_{\odot}$ and $\text{SFR}_{\text{SED}} = 3 - 630 M_{\odot} \text{ yr}^{-1}$, respectively, following the expected MS at $z \sim 5$. There is a good agreement between SFR_{SED} and $\text{SFR}_{\text{UV+IR}}$, as shown by Schaerer et al. (2020). The latter corresponds to the sum of SFR_{UV} , measured from the UV luminosity at 1500 \AA rest-frame (uncorrected for dust attenuation), and SFR_{IR} , measured from the rest-frame $158 \mu\text{m}$ dust continuum emission flux and the FIR SED template of Béthermin et al. (2017) to infer the total IR luminosity (L_{IR}) integrated between $8 \mu\text{m}$ and $1000 \mu\text{m}$ as described in Béthermin et al. (2020). Throughout the paper, we adopt M_{stars} listed in Table A1 of Faisst et al. (2020), based on photometry that includes the *Spitzer* IR imaging, and $\text{SFR}_{\text{UV+IR}}$ derived from the UV magnitudes listed in Table A1 of Faisst et al. (2020) and L_{IR} given in Table B1 of Béthermin et al. (2020). For galaxies undetected in the FIR dust continuum (95 ALPINE galaxies), we consider only SFR_{UV} throughout the paper. Schaerer et al. (2020) discuss in detail the possible amount of SFR_{IR} , the dust-obscured star formation rate, in these 95 ALPINE galaxies and

find that their total SFR can be underestimated by a factor of 1.6, on average, according to the average empirically-calibrated relation between infrared excess ($IRX = L_{IR}/L_{UV}$) and UV spectral slope (β ; $f_{\lambda} \propto \lambda^{\beta}$), derived by Fudamoto et al. (2020) for the ALPINE sample from median stacking of individual continuum images in bins of β . For the majority of the 95 ALPINE galaxies, however, SFR_{IR} turns out to be small ($\lesssim 40\%$ of SFR_{UV}), since their UV spectral slope is fairly blue. We would like to foreshadow that none of our conclusions change when we take the possible underestimation of the total SFR into account.

The ALMA observations were carried out in band 7 during Cycles 5 and 6, and completed in February 2019. Band 7 (275 – 373 GHz) covers the [C II] 158 μm line from $z = 4.1$ to $z = 5.9$, but to avoid an atmospheric absorption no source was included in the redshift range of $z = 4.6$ – 5.1 . Each target was observed for 15–25 minutes of on-source time, with the phase center positioned at the rest-frame UV position of the target and one spectral window in the lower-frequency sideband tuned to the [C II] frequency redshifted by the rest-frame UV spectroscopic redshift of that target (Faisst et al. 2020). The other three spectral windows were used for the FIR continuum around 158 μm rest-frame, close to the FIR SED peak. The ALMA visibility calibration, cleaning, and imaging were performed using the Common Astronomy Software Applications package (CASA; McMullin et al. 2007), as described in detail in Béthermin et al. (2020). The resulting root-mean-square noise (RMS) of the 118 [C II] data cubes ranges between 0.2 mJy beam $^{-1}$ and 0.55 mJy beam $^{-1}$ per 25 km s $^{-1}$ channel for an angular resolution varying between 0.72'' (minimum minor axis) and 1.6'' (maximum major axis). The continuum sensitivity varies with frequency. We reach a mean RMS of 50 $\mu\text{Jy beam}^{-1}$ for ALPINE galaxies at $z = 4.4$ – 4.6, and 28 $\mu\text{Jy beam}^{-1}$ for ALPINE galaxies at $z = 5.1$ – 5.9. The ALMA dataset leads to robust [C II] emission detections for 75 ALPINE galaxies and robust FIR dust continuum emission detections for 23 ALPINE galaxies, with a signal-to-noise ratio (SNR) larger than 3.5 corresponding to 95% purity threshold of both the [C II] line and FIR continuum (Béthermin et al. 2020). Throughout the paper, we consider the 2σ -clipped [C II] fluxes¹, and the FIR continuum fluxes derived using the 2D elliptical Gaussian fits. For the 43 ALPINE targets with no [C II] detections, we consider the “secure” 3σ upper limits² on [C II] fluxes listed in Table C2 of Béthermin et al. (2020).

At the achieved angular resolutions, with an average circularized beam of 0.9'', corresponding to ~ 5.3 – 6.1 kpc at $z = 4.4$ – 5.9, about 2/3 of the ALPINE [C II]-detected galaxies are moderately spatially resolved in the [C II] velocity-integrated intensity maps (Béthermin et al. 2020; Le Fèvre et al. 2020; Fujimoto et al. 2020), meaning their intrinsic (total) sizes as seen in [C II] emission are about the size of the beam, or a significant fraction thereof, as illustrated by the spectacular object studied by Jones et al. (2020). A large diversity of [C II] emission morphologies is observed, from compact/unresolved objects, objects appearing as very extended (Fujimoto et al. 2020; Ginolfi et al. 2020b), to objects showing double, or more, merger-like components (Jones et al. 2020). From our morpho-kinematic visual

classification, described in Le Fèvre et al. (2020), based on the [C II] emission and velocity field and multi-band optical to IR images, we find signatures of possibly interacting systems for 31 ALPINE [C II]-detected galaxies, while only 9 ALPINE galaxies are likely rotation-dominated, indicating that the mass assembly through merging process is frequent at these redshifts for MS SFGs. In what follows, we exclude the 31 galaxies classified as mergers to work with a sample of galaxies where robust measurements of their physical properties can be determined, since deblending the [C II] and dust continuum emissions in closely interacting multi-component systems is difficult with the currently available ALMA data (Béthermin et al. 2020). Therefore, our final sample consists of 87 ALPINE galaxies, of which 44 are detected in [C II], while 43 only have [C II] upper limits.

3. Molecular gas mass estimates

3.1. [C II] as a tracer of cold molecular gas

Zanella et al. (2018) have recently proposed the use of [C II] emission as a tracer of molecular gas by finding a tight empirical correlation, with a 0.3 dex dispersion, between the [C II] luminosity and molecular gas mass derived using mainly the CO tracer (see also Hughes et al. 2017a). This relation seems to hold regardless of the MS or starburst nature of galaxies, redshift (from $z = 0$ to $z = 6$), and metallicity (from $12 + \log(\text{O}/\text{H}) = 7.9$ to $12 + \log(\text{O}/\text{H}) = 8.8$). Zanella et al. (2018) motivate their finding with an explanation of the $L_{\text{CII}}/L_{\text{IR}}$ deficit observed in ultraluminous IR galaxies (ULIRGs) and high-redshift starbursts. Indeed, if L_{CII} traces M_{molgas} (and L_{IR} the SFR), then the [C II] deficit reflects shorter molecular gas depletion timescales in ULIRGs and distant starbursts, consistently with measurements by Daddi et al. (2010) and Genzel et al. (2010).

From the theoretical point of view, the origin of the emission of [C II] is complex, because different ISM phases – ionised, neutral, and molecular – are contributing to it. As a result, one needs to establish whether the fraction of [C II] emission arising from photodissociation regions (PDRs; Stacey et al. 1991; Malhotra et al. 2001; Cormier et al. 2015; Diaz-Santos et al. 2017), produced by the UV radiation from hot stars heating the outer layers of molecular clouds and associated with both the interface layer of neutral gas as well as ionised gas in the H II region itself, is dominating (or not dominating) that arising from the CO photodissociation into C and C $^{+}$ in the cold neutral medium of molecular clouds (Maloney & Black 1988; Madden et al. 1993; Wolfire et al. 2010; Narayanan & Krumholz 2017). In the PDR case C $^{+}$ is rather tracing star formation, while in the CO photodissociation case C $^{+}$ emission emerges from the molecular phase.

The [C II] line has raised considerable interest in galaxies at $z \gtrsim 5$, leading several numerical simulations to model [C II] and to suggest that its emission is dominated at level of > 60 – 85% by molecular clouds more than by diffuse ionised gas (Vallini et al. 2015; Pallottini et al. 2017; Accurso et al. 2017; Olsen et al. 2018). Indeed, CO and [C II] emission maps of the high-redshift galaxy simulated by Vallini et al. (2018) and Pallottini et al. (2017), respectively, clearly show the same morphology with similar spatial distributions on 30 pc scale. In our Milky Way, dense PDRs and CO-dark H $_2$ gas are also the dominant [C II] emitters, responsible for $\sim 55\%$ of the total [C II] emission, while the diffuse ionised gas and diffuse neutral gas contribute to $\sim 20\%$ and $\sim 25\%$, respectively (Pineda et al. 2014; and see also the simulation predictions from Li et al. 2018). As Zanella et al. (2018) warn, when using [C II] as a molecular gas tracer one needs to be aware that since the C $^{+}$ emission might not fully

¹ The 2σ -clipped flux corresponds to the flux integrated within the region around the source defined by the contour level at $\text{SNR} = 2$ in the moment-zero map. The 2σ -clipped fluxes are similar to the 2D-fit fluxes obtained from two-dimensional elliptical Gaussian fits over a $3''$ fitting box around the source (see Fig. 16 in Béthermin et al. 2020).

² The “secure” 3σ upper limits on [C II] fluxes are calculated by adding the 3σ RMS of the noise to the highest flux measured in $1''$ around the phase center in visibility-tapered velocity-integrated flux maps (Béthermin et al. 2020).

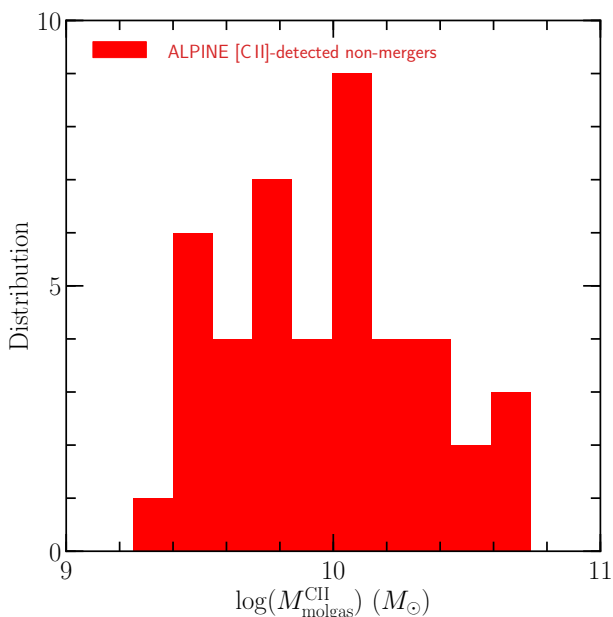


Fig. 1. Distribution of molecular gas masses of the 44 ALPINE [C II]-detected non-merger galaxies at $z = 4.4$ – 5.9 . The molecular gas masses are derived using the calibration of Zanella et al. (2018) between [C II] luminosity and molecular gas mass (Eq. (1)).

emerge from one single gas phase, the measured [C II] luminosity might overestimate the luminosity arising from the molecular gas even in high-redshift galaxies. On the other hand, as C^+ is emitted only in regions where star formation is taking place, the molecular gas not illuminated by stars would not be detected.

Applying the calibration of Zanella et al. (2018) between [C II] luminosity and molecular gas mass:

$$\log\left(\frac{L_{\text{CII}}}{L_{\odot}}\right) = (-1.28 \pm 0.21) + (0.98 \pm 0.02) \log\left(\frac{M_{\text{molgas}}^{\text{CII}}}{M_{\odot}}\right) \quad (1)$$

to the 44 ALPINE [C II]-detected non-merger galaxies with $\log(L_{\text{CII}}/L_{\odot}) = 7.8 - 9.2$, in the regime tested by Zanella et al. (2018), we obtain molecular gas masses in the range of $\log(M_{\text{molgas}}^{\text{CII}}/M_{\odot}) = 9.2 - 10.8$ for these MS SFGs at $z = 4.4 - 5.9$, as shown by the $M_{\text{molgas}}^{\text{CII}}$ distribution in Fig. 1. We calculate the error bars on the [C II]-estimated molecular gas masses by summing in quadrature the relative uncertainty of [C II] fluxes (see Béthermin et al. 2020) and the 0.3 dex dispersion of the $L_{\text{CII}} - M_{\text{molgas}}^{\text{CII}}$ calibration (Zanella et al. 2018).

3.2. Other cold molecular gas mass tracers

In what follows, for a subset of the ALPINE sample we cross-correlate the [C II]-derived molecular gas mass estimates with molecular gas masses inferred using other molecular gas tracers to check the robustness of [C II] as the tracer of cold molecular gas in our sample of $4.4 < z < 5.9$ MS SFGs.

3.2.1. The IR versus CO luminosity relation

We can use the well established empirical relation between IR luminosity and CO(1–0) luminosity measurements (Daddi et al. 2010; Carilli & Walter 2013; Sargent et al. 2014; Dessauges-Zavadsky et al. 2015) to test if the derived $M_{\text{molgas}}^{\text{CII}}$ agree with the measured L_{IR} along the expected relation. This relation,

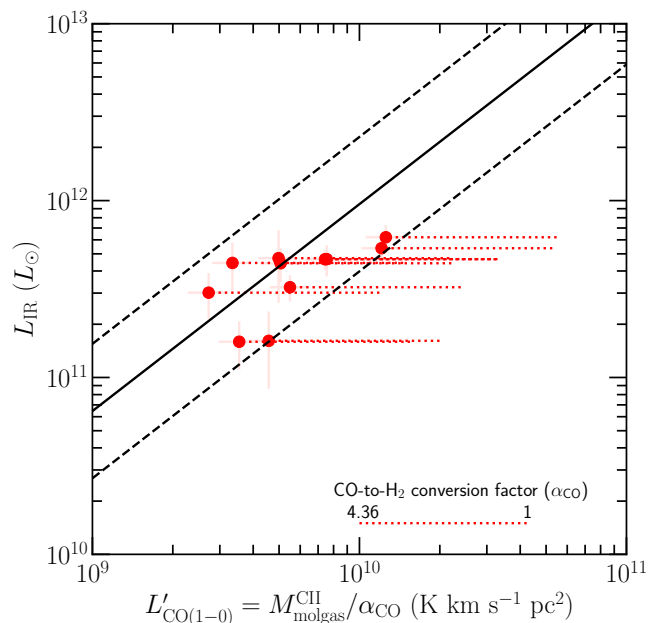


Fig. 2. IR luminosities measured for 11 ALPINE FIR continuum-detected non-merger galaxies (Béthermin et al. 2020) as a function of their CO(1–0) luminosities inferred from the [C II] molecular gas masses and a range of CO-to-H₂ conversion factors (dotted red lines) from the Milky Way value of $4.36 M_{\odot} (\text{K km s}^{-1} \text{pc}^2)^{-1}$ (on the left) to the starburst value of $1 M_{\odot} (\text{K km s}^{-1} \text{pc}^2)^{-1}$ (on the right). The solid black line shows the best-fit of Dessauges-Zavadsky et al. (2015) of the empirical $L_{\text{IR}} - L'_{\text{CO}(1-0)}$ relation with the 1σ dispersion of 0.38 dex (dashed black lines). Within this dispersion the ALPINE [C II]-derived molecular gas masses lie on the relation for the Milky Way α_{CO} .

which spans almost 5 orders of magnitude in L_{IR} from $10^9 L_{\odot}$ to $10^{13.5} L_{\odot}$, was found to be valid for a variety of galaxy types from MS galaxies, starbursts to mergers at redshifts between $z = 0$ and $z \sim 5.3$. In Fig. 2 we show the IR luminosities measured for 11 ALPINE [C II]-detected non-merger galaxies as a function of the CO(1–0) luminosities inferred from the [C II] molecular gas masses and a range of CO-to-H₂ conversion factors (α_{CO}) from the Milky Way value of $4.36 M_{\odot} (\text{K km s}^{-1} \text{pc}^2)^{-1}$ to the starburst value of $1 M_{\odot} (\text{K km s}^{-1} \text{pc}^2)^{-1}$ (Bolatto et al. 2013). We find that for the Milky Way CO-to-H₂ conversion factor all ALPINE galaxies fall within the 0.38 dex dispersion of the IR luminosity versus CO(1–0) luminosity relation, $\log(L_{\text{IR}}/L_{\odot}) = (1.17 \pm 0.03) \log(L'_{\text{CO}(1-0)}/L_{\odot}) + (0.28 \pm 0.23)$, calibrated by Dessauges-Zavadsky et al. (2015), but comparable to Carilli & Walter (2013).

3.2.2. The dust continuum molecular gas masses

At long-wavelengths in the Rayleigh-Jeans tail regime ($\lambda_{\text{rest}} \geq 250 \mu\text{m}$), the thermal dust emission is optically thin and the observed flux density is directly dependent on the mass of dust, the dust opacity coefficient, and the mean temperature of dust contributing to the emission at these wavelengths (Scoville et al. 2016). By assuming that the molecular gas dominates the overall gas budget (the atomic and ionised gas content being negligible) and fixing a dust-to-gas mass ratio, we can then recover the molecular gas mass from the derived dust mass. The rest-frame $850 \mu\text{m}$ luminosity ($L_{850\mu\text{m}}$) was found to exhibit a tight correlation with the ISM molecular gas mass and is now frequently used as a molecular gas tracer (Scoville et al. 2014, 2016, 2017; Hughes et al. 2017b; Privon et al. 2018; Kaasinen et al. 2019).

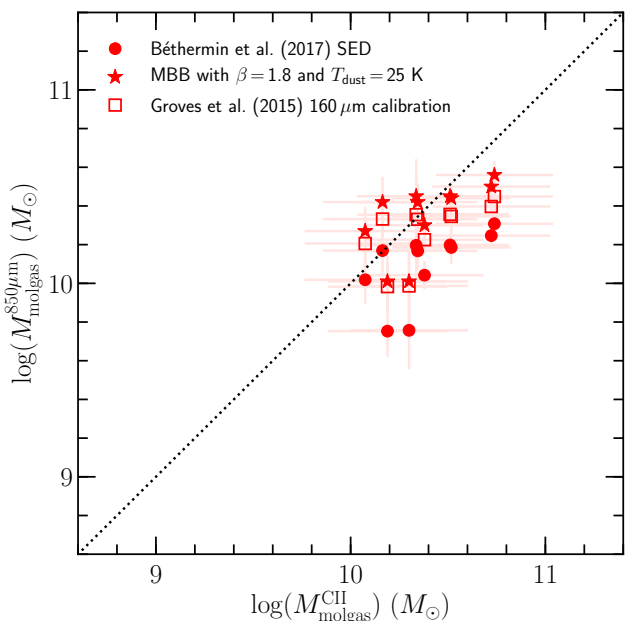


Fig. 3. Comparison of molecular gas masses of the 11 ALPINE FIR continuum-detected non-merger galaxies as derived from the [C II] luminosity (Eq. (1)) and the rest-frame 850 μm luminosity (Eq. (2)). The monochromatic rest-frame 850 μm luminosity is extrapolated from the measured rest-frame 158 μm luminosity by assuming either the FIR SED template of Béthermin et al. (2017) (filled circles), or the MBB curve with $\beta = 1.8$ and $T_{\text{dust}} = 25$ K as adopted by Scoville et al. (2016, 2017) (filled stars). The open squares show the molecular gas masses derived directly from the measured rest-frame 158 μm luminosity using the calibration of Groves et al. (2015), obtained for local galaxies, between *Herschel* PACS 160 μm monochromatic luminosity and gas mass. The dotted line is the one-to-one relation. Overall, there is a good agreement between $M_{\text{molgas}}^{\text{CII}}$ and the different molecular gas masses estimated from the rest-frame 158 μm dust continuum luminosity, even though an average overestimate of 0.3 dex is found when considering the Béthermin et al. (2020) SED (see text for details).

The difficulty remains in deriving $L_{850\mu\text{m}}$ from often a single-band FIR continuum measurement, since this requires us to assume a dust opacity coefficient and a mean dust temperature, or to know the FIR SED characteristic of the studied galaxies.

Béthermin et al. (2020) constructed the mean stacked FIR SEDs specific to ALPINE galaxy analogues, following the same prescriptions as in Béthermin et al. (2015), but using the more recent COSMOS catalogue of Davidzon et al. (2017) and deep SCUBA2 data at 850 μm from Casey et al. (2013). Moreover, the targets to be stacked were selected with properties analogous to the ones of the ALPINE galaxies: $\text{SFR} \gtrsim 10 M_{\odot} \text{ yr}^{-1}$, and redshift bins of $4 < z < 5$ and $5 < z < 6$. The resulting SEDs are best-fit by the Béthermin et al. (2017) SED template, but both the Schreiber et al. (2018) SED template and a modified blackbody (MBB) with dust opacity spectral index fixed to $\beta = 1.8$ and luminosity-weighted dust temperature of 41 ± 1 K at $z < 5$ and 43 ± 5 K at $z > 5$ provide a good fit ($\chi^2 < 4$ for 4 degrees of freedom; see Fig. 9 in Béthermin et al. 2020).

We adopt the Béthermin et al. (2017) FIR SED template to estimate $L_{850\mu\text{m}}$ of the 11 ALPINE non-merger galaxies with FIR continuum detections by scaling the measured monochromatic rest-frame 158 μm luminosity by the ratio between the SED-predicted luminosities at 850 μm and 158 μm . Using then the

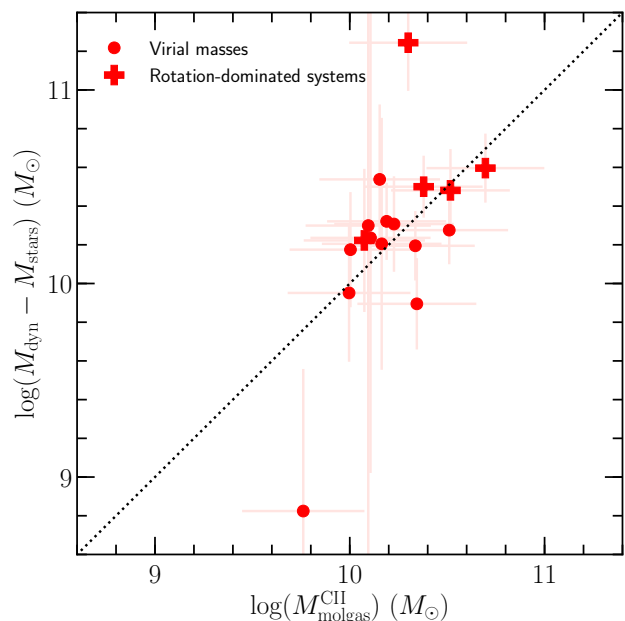


Fig. 4. Comparison of molecular gas masses of ALPINE non-merger galaxies as derived from the [C II] luminosity (Eq. (1)) and the dynamical mass after subtracting M_{stars} (the relative contribution of dark matter is assumed to be negligible). The dynamical masses, accessible only for the ALPINE galaxies with available [C II] size measurements (Fujimoto et al. 2020), are computed using the virial mass definition (Eq. (3); filled circles), except for 5 objects classified as rotation-dominated (Le Fèvre et al. 2020) for which we consider the disk-like gas potential distribution (Eq. (4); crosses). The dotted line is the one-to-one relation. There is a good agreement between $M_{\text{molgas}}^{\text{CII}}$ and molecular gas masses inferred from dynamical masses.

calibration of Kaasinen et al. (2019)³:

$$M_{\text{molgas}}^{850\mu\text{m}} (M_{\odot}) = \left(\frac{L_{850\mu\text{m}}}{\text{erg s}^{-1} \text{ Hz}^{-1}} \right) \left(\frac{1}{6.2 \times 10^{19} (L_{850\mu\text{m}}/10^{31})^{0.07}} \right), \quad (2)$$

we derive the molecular gas masses from the extrapolated rest-frame 850 μm luminosities. These values, although relying on multiple assumptions (e.g., the SED template), are independent measurements to be compared with M_{molgas} inferred from the [C II] luminosity. The comparison is shown in Fig. 3. Within $1 - 2 \sigma$ uncertainty of 0.3 – 0.6 dex, we find an agreement between these two measurements, although there is some trend for a systematic overestimate of $M_{\text{molgas}}^{\text{CII}}$ with respect to $M_{\text{molgas}}^{850\mu\text{m}}$ by 0.3 dex, on average. A similar offset is observed for the Schreiber et al. (2018) SED template and the MBB. On the other hand, when considering the calibration of Groves et al. (2015, Table 5 and $\log(M_{\text{stars}}/M_{\odot}) > 9$), obtained for local galaxies, between monochromatic luminosity in the *Herschel* PACS 160 μm band and gas mass, which relies on much fewer assumptions, we find only a marginal overestimate by 0.1 dex of $M_{\text{molgas}}^{\text{CII}}$ relative to these gas mass estimates (open squares).

The observed $M_{\text{molgas}}^{\text{CII}}$ overestimate with respect to $M_{\text{molgas}}^{850\mu\text{m}}$ may be attributed to three possible effects. First, it points to po-

³ The calibration of Kaasinen et al. (2019) is comparable to the calibration of Scoville et al. (2016) with a constant $\alpha_{850\mu\text{m}} = L_{850\mu\text{m}}/M_{\text{molgas}}^{850\mu\text{m}} = (6.7 \pm 1.7) \times 10^{19} \text{ erg s}^{-1} \text{ Hz}^{-1} M_{\odot}^{-1}$, although it shows some deviations at $L_{850\mu\text{m}} \lesssim 5 \times 10^{30} \text{ erg s}^{-1} \text{ Hz}^{-1}$, but which remains well within the scatter of data used to establish the calibrations.

tential contributions from the neutral atomic and ionised phases to the measured [C II] emission, in addition to the molecular gas phase. Second, it suggests that the calibration of Kaasinen et al. (2019) may not be valid for the ALPINE galaxies at $z \gtrsim 4.5$. Remember that the Scoville et al. (2014) method assumes a constant dust-to-gas mass ratio of $\sim 1 : 100$, as also supported by Kaasinen et al. (2019). Yet we may expect a lower dust-to-gas mass ratio ($\propto \alpha_{850\mu\text{m}}$ in Eq. (2)) for the ALPINE galaxies, since ALPINE galaxies have lower M_{stars} (with a median of $10^{9.7} M_{\odot}$) than SFGs with $M_{\text{stars}} > 10^{10.3} M_{\odot}$ studied by Scoville et al. (2016) and Kaasinen et al. (2019) and are deficient in dust obscured star-formation activity with respect to lower redshift SFGs as found by Fudamoto et al. (2020). To reconcile $M_{\text{molgas}}^{850\mu\text{m}}$ with $M_{\text{molgas}}^{\text{CII}}$, $\alpha_{850\mu\text{m}}$ would need to be lower by a factor of ~ 2 . Third, it supports that the SED in the Rayleigh-Jeans tail out to $850 \mu\text{m}$ rest-frame could be dominated by a cold component. When fixing the dust opacity spectral index to $\beta = 1.8$ and considering this time a mass-weighted dust temperature of $T_{\text{dust}} = 25 \text{ K}$ in the MBB SED parametrization, similarly to Scoville et al. (2016, 2017), which we use to extrapolate the $158 \mu\text{m}$ luminosity to the $850 \mu\text{m}$ luminosity, we obtain comparable gas masses (filled stars in Fig. 3) to $M_{\text{molgas}}^{\text{CII}}$.

3.2.3. The dynamical masses

As discussed in Le Fèvre et al. (2020), 2/3 of the ALPINE [C II]-detected galaxies are moderately spatially resolved. For a subset of 18 non-merger galaxies with high-SNR ($\gtrsim 5$) [C II] detections, Fujimoto et al. (2020) derived their [C II] sizes by performing exponential-disk profile fits in the visibility plane with UVMULTIFIT (Martí-Vidal et al. 2014). The circularized effective radii (r_e), defined as the square-root of the product of the effective major and minor axes, are adopted as size measurements and are listed in Table 1 of Fujimoto et al. (2020). For the ALPINE galaxies with size measurement, we can derive their dynamical mass under the assumption that the gas potential structure of ALPINE galaxies arises in a virialised spherical system of radius equal to the measured circularized effective radius and with the one-dimensional velocity dispersion (σ_{CII}) inferred from the full-width half maximum ($\text{FWHM}_{\text{CII}}^{\text{intrinsic}}$) of the [C II] line corrected for final channel spacing⁴:

$$M_{\text{dyn}}^{\text{virial}} (M_{\odot}) = 1.56 \times 10^6 \left(\frac{\sigma_{\text{CII}}}{\text{km s}^{-1}} \right)^2 \left(\frac{r_e}{\text{kpc}} \right), \quad (3)$$

following Eq. (10) in Bothwell et al. (2013). This virialised spherical geometry dynamical mass is 0.13 dex larger than the dynamical mass we would obtain if we assumed a disk-like gas potential distribution for the same source size, the same $\text{FWHM}_{\text{CII}}^{\text{intrinsic}}$, and a mean inclination angle of the source of $\langle \sin i \rangle = \pi/4$ (Law et al. 2009; Wang et al. 2013; Capak et al. 2015). But, the virial mass has the advantage of avoiding to add the supplementary uncertainty on the source orientation needed in the computation of the dynamical mass for disk geometry. For 5 out of the 9 ALPINE galaxies classified as rotation-dominated systems (Le Fèvre et al. 2020), we obtained robust [C II] minor and major axis ratio measurements (Fujimoto et al. 2020), which enable us to constrain their disk inclination angle (i) as $i = \cos^{-1}(\text{minor/major})$. For these 5 galaxies, we also compute

⁴ $\text{FWHM}_{\text{CII}}^{\text{intrinsic}} = \sqrt{\text{FWHM}_{\text{CII}}^{\text{observed}}{}^2 - 25^2}$, where 25 km s^{-1} is the spectral resolution that, in our spectral configuration, equals the final channel spacing (ALMA Technical Handbook). We then obtain the velocity dispersion from $\sigma_{\text{CII}} = \text{FWHM}_{\text{CII}}^{\text{intrinsic}} / \sqrt{8 \ln(2)}$.

their dynamical mass for the disk-like gas potential distribution:

$$M_{\text{dyn}}^{\text{rotation}} (M_{\odot}) = 1.16 \times 10^5 \left(\frac{v_{\text{cir}}}{\text{km s}^{-1}} \right) \left(\frac{2r_e}{\text{kpc}} \right), \quad (4)$$

where the circular velocity of the gaseous disk is $v_{\text{cir}} = 1.763 \sigma_{\text{CII}} / \sin(i)$. The corresponding dynamical masses are randomly scattered by up to ± 0.25 dex from virial masses.

Since the relative contribution of dark matter in the internal regions of galaxies (at $< (1 - 2)r_e$) is expected to be low (Barnabè et al. (2012) report a dark matter fraction within $2.2r_e$ of at most $0.28^{+0.15}_{-0.10}$), the dynamical mass may be assumed to reflect the total baryonic mass, which can be used to obtain an estimate of M_{molgas} after subtracting M_{stars} . Out of the 18 ALPINE non-merger galaxies with size measurements, for one galaxy⁵ the virial mass ends up to be smaller than its M_{stars} . For the remaining 17 ALPINE galaxies, we can cross-match the molecular gas masses obtained from their dynamical and stellar masses with the gas masses inferred from their [C II] luminosity. For 12 ALPINE galaxies we consider the virial masses, and for the 5 ALPINE galaxies classified as rotation-dominated we consider the dynamical masses derived for a disk-like gas potential. As shown in Fig. 4, there is a good agreement within the 1σ uncertainty of 0.3 dex between these respective molecular gas mass estimates, except for two outliers (they do not show any systematic trend). A good one-to-one relationship between the two molecular gas mass estimates was expected, since the dynamical mass, if tracing the baryonic mass only (no dark matter), accounts for M_{stars} plus the total gas mass that includes all gas phases (molecular, atomic, ionised) as likely does the [C II] emission.

4. Comparison sample

Tremendous observational efforts have been dedicated to determine the molecular gas content of galaxies from the present day to high redshift, using either the CO emission or the FIR dust continuum as molecular gas mass tracers. These tracers have their respective strengths and uncertainties (see Bolatto et al. 2013; Genzel et al. 2015; Scoville et al. 2016; Tacconi et al. 2018). While the former tracer is the most commonly used and well-calibrated tracer in the local Universe, the latter tracer, which usually relies on a single-band measurement preferably in the Rayleigh-Jeans tail of the FIR SED, is particularly cheap in terms of ALMA observing time. Here we propose to compare the ALPINE $M_{\text{molgas}}^{\text{CII}}$ with a compilation of local to high-redshift MS SFGs with molecular gas masses derived from CO luminosity measurements reported in the literature.

We build up the database of CO-detected MS SFGs starting from the exhaustive compilation of CO luminosity measurements in MS SFGs at $z > 1$ presented in Dessauges-Zavadsky et al. (2015, 2017). We extend this compilation with CO measurements at $z > 1$ published since 2015⁶ by Seko et al. (2016), Papovich et al. (2016), González-López et al. (2017), Magdis et al. (2017), Valentino et al. (2018), Gowardhan et al. (2019), Kaasinen et al. (2019), Molina et al. (2019), Aravena et al.

⁵ In VUDS COSMOS 5101218326 the virial mass is smaller than M_{stars} , likely because of an overestimation of M_{stars} given the distorted morphology of the galaxy in the *Hubble* Space Telescope optical bands (Faisst et al. 2020), although we cannot exclude an underestimation of its virial mass as well.

⁶ We do not include the CO detection of D’Odorico et al. (2018) in our compilation of CO-detected MS SFGs, because M_{stars} of the corresponding galaxy is not known.

(2019), Bourne et al. (2019), Pavesi et al. (2019), and Cas-sata et al. (2020). And we include the release of the NOEMA PHIBSS2 legacy survey at $0.5 < z < 2.5$, described in Tacconi et al. (2018) and Freundlich et al. (2019). We adopt the MS parametrization from Speagle et al. (2014, Eq. (28)), similarly to what was done for PHIBSS2, and retain only SFGs lying within the MS dispersion of $\Delta_{\text{MS}} = \log(\text{SFR}/\text{SFR}_{\text{MS}}) = \pm 0.3$ dex. The updated compilation comprises a total of 101 CO luminosity measurements of MS SFGs at $1 < z < 3.7$ and with $M_{\text{stars}} = 10^{9.5} - 10^{11.7} M_{\odot}$, plus the CO detection at $z = 5.65$ from Pavesi et al. (2019), but is still under-sampled at high-redshift ($z > 2.5$) and at the low- M_{stars} end ($M_{\text{stars}} < 10^{10} M_{\odot}$). The compilation of Dessauges-Zavadsky et al. (2015) also contained CO(1–0) measurements for a non-exhaustive number of local spiral galaxies and MS SFGs at $z < 1$. We now add the CO(1–0) measurements from the final xCOLD GASS survey at $0.01 < z < 0.05$ performed with the IRAM 30 m telescope (Saintonge et al. 2016, 2017), which now extends to lower M_{stars} than in previous samples, i.e. $\log(M_{\text{stars}}/M_{\odot}) = 9 - 10$.

At $z > 0.5$, the CO(1–0) transition is often replaced by a high- J CO transition with $J = 2$ to 5, which requires the calibration of temperature and density from the CO spectral line energy distribution (CO SLED) to access the CO luminosity correction factor $r_{J,1} = L'_{\text{CO}(J \rightarrow J-1)}/L'_{\text{CO}(1-0)}$. CO SLED observations in MS SFGs at $z \sim 1 - 3.7$ converge toward $r_{2,1} = 0.81 \pm 0.15$, $r_{3,1} = 0.57 \pm 0.11$, $r_{4,1} = 0.33 \pm 0.06$, and $r_{5,1} = 0.23 \pm 0.04$ (Daddi et al. 2015; Dessauges-Zavadsky et al. 2015, 2019; Cas-sata et al. 2020). In order to have a homogeneous comparison sample, we adopt these CO luminosity correction factors to all CO $J \rightarrow J - 1$ luminosity measurements in our compilation, and we derive the molecular gas masses, $M_{\text{molgas}} = \alpha_{\text{CO}}^Z \left(\frac{L'_{\text{CO}(J \rightarrow J-1)}}{r_{J,1}} \right)$, assuming the same CO-to- H_2 metallicity-dependent conversion function:

$$\alpha_{\text{CO}}^Z (M_{\odot}(\text{K km s}^{-1} \text{ pc}^2)^{-1}) = \alpha_{\text{CO,MW}} \times \sqrt{0.67 \exp(0.36 \times 10^{-(12+\log(\text{O}/\text{H})-8.67)})} \times \sqrt{10^{-1.27(12+\log(\text{O}/\text{H})-8.67)}}, \quad (5)$$

which corresponds to the geometrical mean of the metallicity-dependent conversion functions of Bolatto et al. (2013) and Genzel et al. (2012), following Eq. (2) in Tacconi et al. (2018). We adopt the Milky Way CO-to- H_2 conversion factor of Strong & Mattox (1996), $\alpha_{\text{CO,MW}} = 4.36 M_{\odot}(\text{K km s}^{-1} \text{ pc}^2)^{-1}$, which includes the correction factor of 1.36 for helium. To estimate the metallicities of the CO-detected SFGs when direct metallicity measurements are not available, we use the redshift-dependent mass-metallicity relation defined by Genzel et al. (2015)⁷, calibrated to the Pettini & Pagel (2004) metallicity scale and the solar abundance of $12 + \log(\text{O}/\text{H})_{\odot} = 8.67$ (Asplund et al. 2004):

$$12 + \log(\text{O}/\text{H})_{\text{pp04}} = a - 0.087(\log(M_{\text{stars}}) - b)^2 \quad (6)$$

with $a = 8.74$ and $b = 10.4 + 4.46 \log(1+z) - 1.78(\log(1+z))^2$. As discussed in Dessauges-Zavadsky et al. (2017), α_{CO}^Z increases with redshift for any given M_{stars} , and at any given redshift increases with decreasing M_{stars} . As a result, α_{CO}^Z might be particularly uncertain at high redshifts ($z \gtrsim 3$) and for small M_{stars}

⁷ The redshift-dependent mass-metallicity relation of Genzel et al. (2015) was constructed by combining mass-metallicity relations at different redshifts presented by Erb et al. (2006), Maiolino et al. (2008), Zahid et al. (2014), and Wuyts et al. (2014).

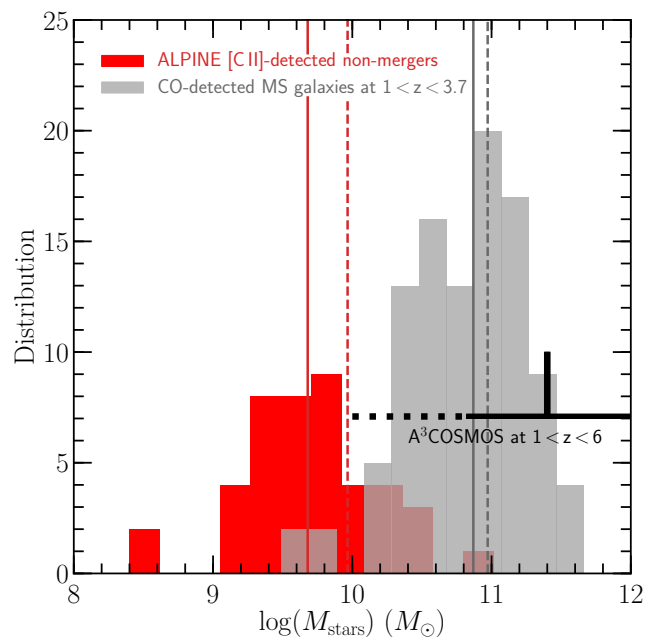


Fig. 5. Distribution of stellar masses of the 44 ALPINE [C II]-detected non-merger galaxies at $z = 4.4 - 5.9$ (red histogram) and the comparison sample of 101 CO-detected MS SFGs at $1 < z < 3.7$ compiled from the literature (grey histogram). The solid and dashed lines correspond, respectively, to the medians and means of the two distributions. The black thick lines show the range and the mean of M_{stars} of the A³COSMOS galaxies at $1 < z < 6$ (Liu et al. 2019b). Clearly, the ALPINE sample probes a much lower M_{stars} range than previous galaxy samples with molecular gas mass measurements obtained mostly at lower redshifts.

($M_{\text{stars}} \lesssim 10^{10} M_{\odot}$), because of the less constrained mass-metallicity relation in this range of physical parameters.

Finally, to check if our compilation of high-redshift SFGs at $0.1 < z < 3.7$ with molecular gas masses derived from CO luminosity measurements is representative of MS SFGs at these redshifts, we consider the mean M_{molgas} obtained by Béthermin et al. (2015) from their stacking analysis of the IR to millimeter emission of MS SFGs, with an average M_{stars} of $\sim 10^{10.8} M_{\odot}$, blindly selected in the COSMOS field between $z = 0.25$ and $z = 4$. For a coherent comparison, we rescale the molecular gas masses of Béthermin et al. (2015) to the mass-metallicity relation used in the CO compilation (Eq. (6)). Nevertheless, we keep the metallicity correction of $0.3 \times (1.7 - z)$ dex they applied at $z > 1.7$ and which becomes significant for galaxies beyond $z > 2.5$. We find that the respective molecular gas depletion timescales and gas fractions globally agree, supporting that the sample of CO-detected SFGs is unbiased, except maybe in the redshift bin of $1 < z < 1.5$ where the CO-measured molecular gas masses tend to be higher than the Béthermin et al. (2015) FIR SED stack results (see Fig. 6, left panel and Fig. 8, top panel).

Recently, Liu et al. (2019b) published M_{molgas} measurements for about 700 galaxies at $0.3 < z < 6$, extracted on an automated prior-based and blind-based ALMA Archive mining in the COSMOS field (hereafter A³COSMOS, with spectroscopic redshifts available for 36% of the sample (Liu et al. 2019a)). The molecular gas masses were derived from single-band FIR continuum and multi-wavelength FIR SEDs. The A³COSMOS galaxies, however, are mostly probing the high M_{stars} domain of MS SFGs at $z > 1$ with $M_{\text{stars}} \sim 10^{11} - 10^{12} M_{\odot}$. They thus are, on average, 10 – 100 times more massive than the ALPINE [C II]-detected galaxies that have a median M_{stars} of $\sim 10^{9.7} M_{\odot}$

(and a mean of $\sim 10^{10} M_{\odot}$). Consequently, in terms of the respective M_{stars} distributions shown in Fig. 5, our compilation of CO-detected MS galaxies at $z > 1$ represents a better comparison sample for the ALPINE galaxies, despite the fact that in the redshift range of ALPINE galaxies ($z = 4.4 - 5.9$) one single CO detection is included, against 24 M_{molgas} measurements for MS SFGs in the A³COSMOS sample. With a median M_{stars} of $\sim 10^{10.9} M_{\odot}$ (and a mean of $\sim 10^{11} M_{\odot}$), the CO-detected SFGs globally have adequate masses at $1 < z < 3.7$ to plausibly be the descendants of the ALPINE galaxies according to the multi-epoch abundance matching simulations (Behroozi et al. 2013, 2019; Moster et al. 2013, 2018), as discussed in Sect. 5.3.

5. Analysis and discussion

The comparison of the molecular gas masses inferred from the [C II] luminosity, following the calibration proposed by Zanella et al. (2018), with three independent gas mass tracers discussed in Sect. 3.2 yields reassuring results supporting [C II] as a statistically reliable tracer of cold molecular gas for the ALPINE galaxies. The [C II]-estimated gas masses are associated with large error bars (~ 0.3 dex), but these error bars appear to be comparable to those of other tracers. In what follows, we adopt the [C II] gas masses derived for the ALPINE galaxies to study the evolution of the molecular gas content of MS SFGs up to $z \sim 6$. We stress that if instead we choose another of the tested molecular gas mass tracers, we would obtain similar conclusions.

5.1. Molecular gas depletion timescale

From estimates of M_{molgas} and SFR of galaxies, we can infer their molecular gas depletion timescale, defined as $t_{\text{depl}} = M_{\text{molgas}}/\text{SFR}$. This gas depletion timescale (or gas consumption timescale) describes how long each galaxy may sustain star formation at the measured rate before running out of molecular gas fuel under the assumption that the gas reservoir is not replenished. Since the earliest CO luminosity measurements in high-redshift MS SFGs, there has been evidence for shorter t_{depl} at high redshift, such that $t_{\text{depl}} \sim 1 - 2$ Gyr observed at $z = 0$ (e.g., Bigiel et al. 2008; Leroy et al. 2013; Saintonge et al. 2017) drops by a factor of ~ 2 at $z \sim 2.5$ (e.g., Tacconi et al. 2013, 2018, 2020; Saintonge et al. 2013; Genzel et al. 2015; Béthermin et al. 2015; Dessauges-Zavadsky et al. 2015, 2017; Schinnerer et al. 2016; Scoville et al. 2017; Liu et al. 2019b). Shorter t_{depl} correspond to higher star formation efficiencies (SFE = $1/t_{\text{depl}}$) that are taking place in high-redshift galaxies, efficient enough to exhaust similar and even larger gas reservoirs over a shorter timescale than in nearby MS SFGs. The so-far inferred t_{depl} evolution with redshift, up to $z \sim 3.5$, nevertheless appears much shallower than $t_{\text{depl}} \sim (1+z)^{-1.5}$ (see Fig. 6, left panel) that is predicted by semi-analytical and cosmological simulations developed in the framework of the bathtub model (e.g. Davé et al. 2011, 2012; Genel et al. 2014; Lagos et al. 2015). This suggests that distant galaxies either intrinsically do not have such high SFE, or are more gas-rich than predicted, or outflows, if highly mass loaded, contribute to reduce the gas.

The ALPINE sample enables us, for the first time, to explore the t_{depl} evolution beyond $z \gtrsim 4.5$ for a statistically significant number of MS SFGs with a median M_{stars} of $10^{9.7} M_{\odot}$. The measured t_{depl} means and errors in two redshifts bins of $4.4 < z < 4.6$ and $5.1 < z < 5.9$ are listed in Table 1. We provide both the means obtained when considering only the 44 [C II]-detected galaxies and when also taking into account the “secure” 3σ up-

Table 1. ALPINE molecular gas depletion timescale and molecular gas fraction means in two redshift bins

	$4.4 < z < 4.6$	$5.1 < z < 5.9$
$\langle t_{\text{depl}} \rangle$ detections	5.8 ± 0.6	4.6 ± 0.8
$\langle t_{\text{depl}} \rangle$ detections+limits	2.3 ± 0.3	2.3 ± 0.4
$\langle f_{\text{molgas}} \rangle$ detections	0.67 ± 0.03	0.59 ± 0.05
$\langle f_{\text{molgas}} \rangle$ detections+limits	0.46 ± 0.05	0.46 ± 0.05

Notes. $\langle t_{\text{depl}} \rangle$ values are in 10^8 yr. The detections refer to the 44 ALPINE [C II]-detected non-merger galaxies and the limits to the “secure” 3σ upper limits of the 43 [C II]-non-detected galaxies (see Sect. 2).

per limits of the 43 galaxies undetected in [C II] (see Sect. 2). The latter means are computed using the survival analysis (with routines described in Isobe et al. 1986). In particular, we use the Kaplan-Meier estimator, an unbiased non-parametric maximum likelihood estimator that determines the characteristic of a parent population with no assumption on the distribution of the parent population from which the censored sample is drawn (see also Talia et al. 2020). The respective t_{depl} means without/with limits differ by about a factor of 2.

In Fig. 6 (left panel) we show the molecular gas depletion timescale as a function of redshift for the ALPINE [C II]-detected non-merger galaxies (red circles) and [C II]-non-detected galaxies (light-red arrows) distributed in the redshift bins of $4.4 < z < 4.6$ and $5.1 < z < 5.9$, and for our compilation of CO-detected MS SFGs from the literature separated in 6 redshift bins of $z = 0$, $0 < z < 0.1$, $0.1 < z < 1$, $1 < z < 1.5$, $1.5 < z < 2.5$, and $2.5 < z < 3.7$, chosen in the way that the three bins between $z = 0.1$ and $z = 2.5$ contain a comparable number of galaxies (~ 40). We then compute the respective means, errors on the mean, and standard deviations per redshift bin (black/grey big crosses). We show the ALPINE means obtained for the 44 [C II] detections (see Table 1). We also overplot the depletion timescales obtained by Béthermin et al. (2015) from FIR SED stacks (light-grey shaded area). We observe a continuous decline of t_{depl} from $z = 0$ to $z = 5.9$. The decline follows a power-law with a slope clearly shallower than $(1+z)^{-1.5}$ (dotted line), as this latter would imply $t_{\text{depl}} = 6.0 \times 10^7$ yr at $z = 5.5$ when fixing the zero-point at $z = 0$ to 1 Gyr. This predicted t_{depl} value is comparable to the smallest ALPINE t_{depl} measurement, but is almost one order of magnitude shorter than the mean t_{depl} of $(4.6 \pm 0.8) \times 10^8$ yr of the ALPINE [C II]-detected non-merger galaxies in the redshift bin of $5.1 < z < 5.9$. Even if, for the ALPINE galaxies undetected in the FIR continuum emission, we add to their measured SFR_{UV} the possible SFR_{IR} contribution, estimated using the ALPINE IRX- β relation obtained from stacking (Fudamoto et al. 2020) as discussed in Sect. 2, the resulting mean t_{depl} of $\sim 3.8 \times 10^8$ yr over $4.4 < z < 5.9$ is still too long compared to the $(1+z)^{-1.5}$ decline. When taking into account the “secure” 3σ upper limits of the ALPINE galaxies undetected in [C II], the mean t_{depl} drops to $(2.3 \pm 0.4) \times 10^8$ yr in the redshift bin of $5.1 < z < 5.9$. This drop suggests a steeper t_{depl} decrease with redshift than shown by [C II] detections, but the reached mean t_{depl} value is still a factor of ~ 4 longer than for the predicted one. Consequently, on average, MS SFGs at $z \gtrsim 4.5$ are not considerably more efficient in forming stars than those galaxies at $z \sim 2 - 3$, as also supported by the low SFE obtained by Pavesi et al. (2019) from the CO(2–1) molecular gas mass measurement in a MS SFG at $z = 5.65$ (see the blue triangle at $z = 5.65$ in the left panel of Fig. 6).

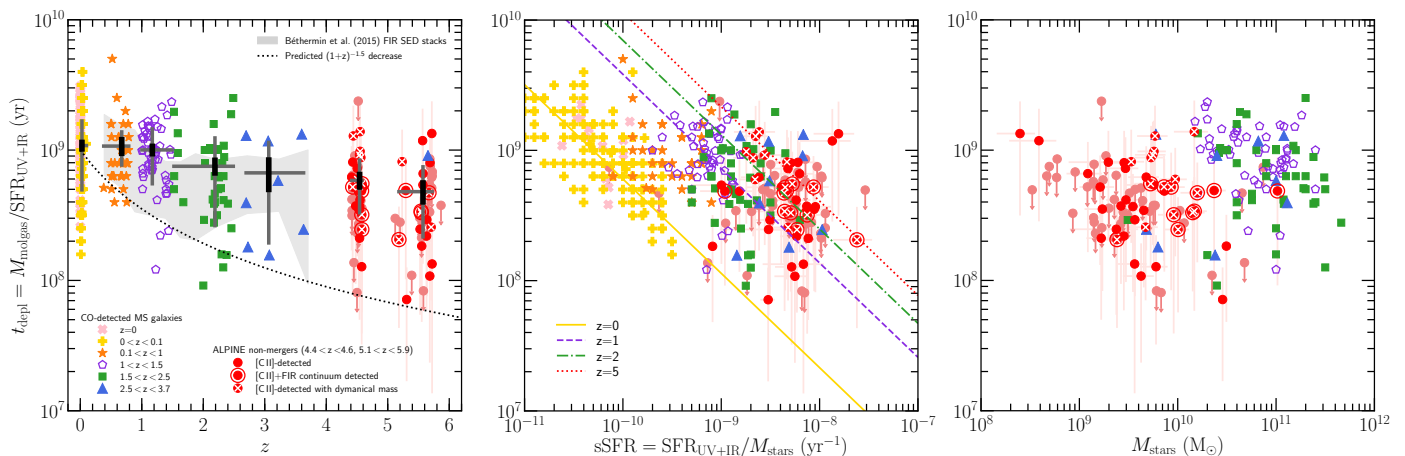


Fig. 6. Molecular gas depletion timescales plotted for the ALPINE non-merger galaxies distributed in two redshift bins of $4.4 < z < 4.6$ and $5.1 < z < 5.9$ (red circles; encircled red circles mark the ALPINE galaxies detected in FIR dust continuum; crossed red circles mark the ALPINE galaxies with dynamical mass measurements; and light-red arrows correspond to 3σ upper limits) and for our compilation of CO-detected MS SFGs from the literature color-coded in 6 redshift bins of $z = 0$ (pink crosses), $0 < z < 0.1$ (yellow pluses), $0.1 < z < 1$ (orange stars), $1 < z < 1.5$ (violet open pentagons), $1.5 < z < 2.5$ (green squares), and $2.5 < z < 3.7$ (blue triangles, plus the Pavesi et al. (2019) object at $z = 5.65$). *Left panel.* Molecular gas depletion timescales shown as a function of redshift. The respective means, errors on the mean, and standard deviations per redshift bin are indicated by the black/grey big crosses. The light-grey shaded area corresponds to the depletion timescales obtained by Béthermin et al. (2015) from FIR SED stacks. The t_{depl} means per redshift bin follow a decrease out to $z \sim 6$, but much shallower than the $(1+z)^{-1.5}$ decline predicted in the framework of the bathtub model (dotted line). *Middle panel.* Molecular depletion timescales shown as a function of specific star formation rate. A strong anti-correlation between t_{depl} and sSFR is observed at $z = 0$ (yellow solid line from Saintonge et al. 2011) and at high redshift. The displacement along the sSFR-axis for galaxies at higher redshifts is compatible with the sSFR evolution with redshift (violet dashed line at $z = 1$, green dashed-dotted line at $z = 2$, and red dotted line at $z = 5$, as computed using the sSFR(z) parametrization from Speagle et al. 2014, Eq. (28)). *Right panel.* Molecular depletion timescales, restricted to $z \sim 1 - 5.9$ SFGs, shown as a function of M_{stars} . No correlation between t_{depl} and M_{stars} is observed for SFGs at $z \sim 1 - 5.9$.

There is a significant scatter, larger than 1 dex, among the t_{depl} measurements in all redshift bins, even though we only consider MS galaxies with $\Delta\text{MS} = \pm 0.3$ dex around the MS parametrization of Speagle et al. (2014). This scatter at a fixed redshift is believed to be a product of the multi-functional dependence of t_{depl} on many physical parameters, such as the offset from the MS, the star formation rate, the stellar mass, and possibly the environment (e.g., Dessauges-Zavadsky et al. 2015; Scoville et al. 2017; Noble et al. 2017; Silverman et al. 2018; Tacconi et al. 2018; Tadaki et al. 2019; Liu et al. 2019b). Given the strong anti-correlation found between t_{depl} and the offset from the MS (Genzel et al. 2015; Dessauges-Zavadsky et al. 2015; Tacconi et al. 2018), we still expect t_{depl} variations for galaxies on the MS while in their evolutionary process they are transiting up and down across the MS band (e.g., Sargent et al. 2014; Tacchella et al. 2016). The previously reported anti-correlation between t_{depl} and sSFR (Saintonge et al. 2011; Dessauges-Zavadsky et al. 2015) is also further supported by our galaxies at $z = 4.4 - 5.9$ (Fig. 6, middle panel). It highlights comparable timescales for gas consumption and stellar mass formation (Saintonge et al. 2011; Dessauges-Zavadsky et al. 2015). We find a Spearman rank coefficient of -0.49 and p -value of 4.5×10^{-10} for the dependence of t_{depl} on sSFR when considering the MS SFGs at $z \sim 1 - 5.9$. The observed offset of ALPINE galaxies with respect to the t_{depl} -sSFR relation of MS SFGs at $z = 0$ and to a lesser extent to the relations at $z \sim 1$ and $z \sim 2$ agrees with the displacement of the $z = 0$ relation along the sSFR-axis by factors derived from the redshift evolution of sSFR of MS SFGs out to redshifts of $z \sim 5$ (Speagle et al. 2014), although a less steep sSFR redshift evolution toward $z \sim 5$ than parametrised by Speagle et al. (2014) is suggested in line with the sSFR(z) results of Khusanova et al. (2020b). With t_{depl} measurements achieved down to $M_{\text{stars}} \sim 10^{8.4} M_{\odot}$ for the ALPINE

galaxies, we confirm, on the other hand, that for MS SFGs at $z \sim 1 - 5.9$ the t_{depl} dependence on M_{stars} , if any, must be weak as shown in Fig. 6 (right panel). This supports that the linear Kennicutt-Schmidt relation established for local galaxies (Kennicutt 1998a) might hold up to $z \sim 5.9$ MS SFGs.

Scoville et al. (2017), Tacconi et al. (2018), and Liu et al. (2019b) performed, for their respective compilations of galaxies with M_{molgas} measurements, a multi-functional fitting to simultaneously quantify the underlying dependency of t_{depl} as products of power laws in redshift, M_{stars} , and offset from the MS (as well as optical size in the case of Tacconi et al. (2018), who ultimately found a negligible t_{depl} dependence on size). They used slightly different criteria in their fitting procedure, but assumed the same MS parametrization from Speagle et al. (2014, Eq. (28))⁸. Their respective best-fits yield different t_{depl} functional forms, which are compared in Liu et al. (2019b). While the Tacconi et al. (2018) t_{depl} function was fitted with data covering only redshifts of $z \sim 0 - 3$, the Liu et al. (2019b) function does account for data at $z > 3$, but restricted to MS SFGs with high M_{stars} ($M_{\text{stars}} \sim 10^{11} M_{\odot}$). The three fitted functions in fact lack constraints for MS low mass ($M_{\text{stars}} \lesssim 10^{10} M_{\odot}$) SFGs at $z > 3$. These SFGs are particularly important, since, as shown by Liu et al. (2019b), the largest differences between the three fitted t_{depl} functions are observed for MS SFGs at $z > 4$ with $M_{\text{stars}} < 10^{10} M_{\odot}$. The ALPINE galaxies are precisely characterised by these physical properties and can therefore bring decisive constraints on the t_{depl} function.

In Fig. 7 (top panels) we show, similarly to Liu et al. (2019b), the molecular gas depletion timescale as a function of redshift

⁸ To be exact, Scoville et al. (2017) used a combination of MS parametrizations from Speagle et al. (2014) and Lee et al. (2015), but this combination only affects SFGs with high $M_{\text{stars}} \gtrsim 10^{10.5} M_{\odot}$. Below this mass threshold, the Speagle et al. (2014) MS parametrization holds.

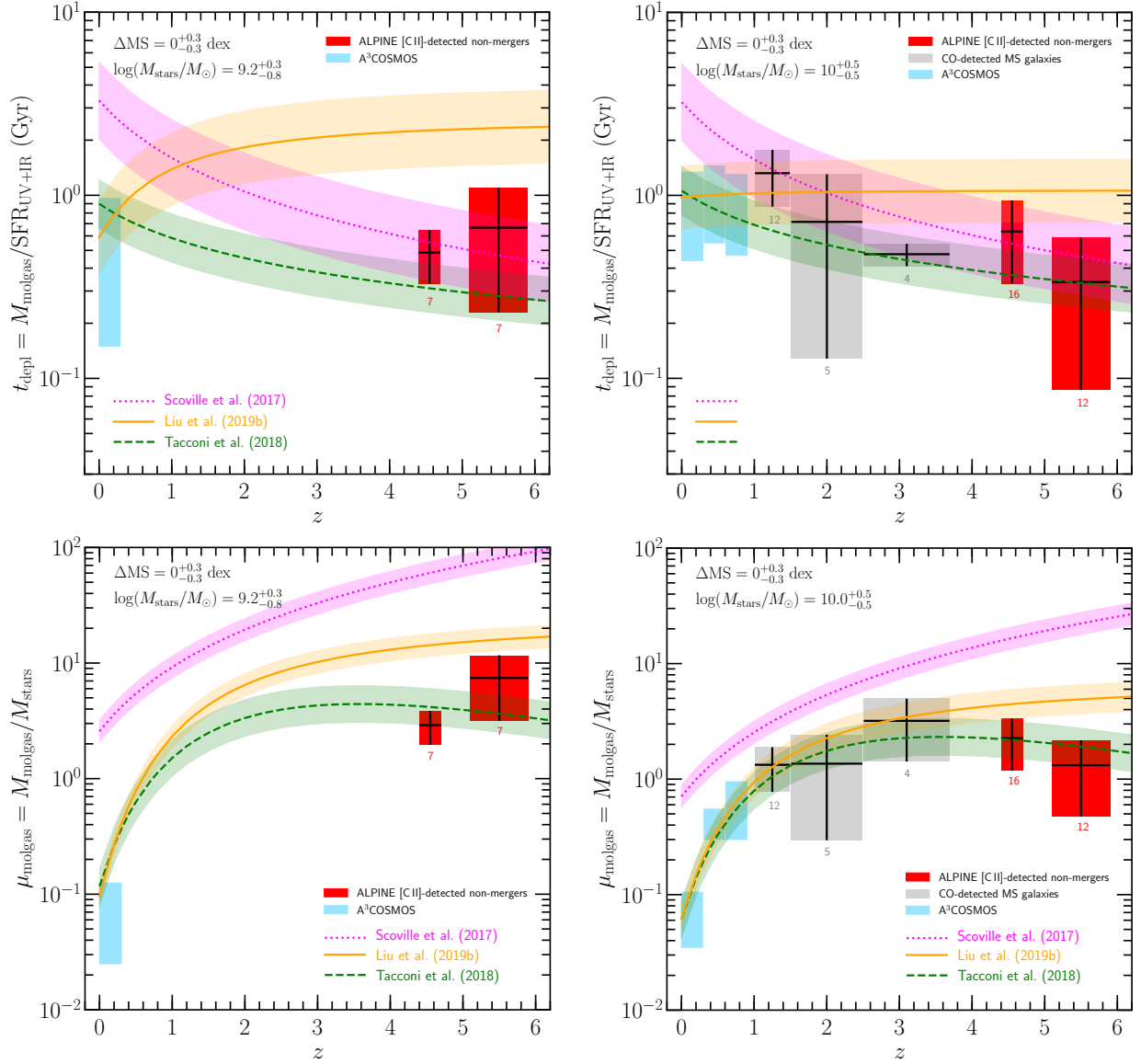


Fig. 7. Redshift evolution of the molecular depletion timescale (*top panels*) and the molecular gas mass to stellar mass ratio (*bottom panels*) of MS galaxies ($\Delta MS = 0_{-0.3}^{+0.3}$ dex) in two stellar mass bins of $\log(M_{\text{stars}}/M_{\odot}) = 8.4 - 9.5$ (*left panels*) and $\log(M_{\text{stars}}/M_{\odot}) = 9.5 - 10.5$ (*right panels*). The red boxes show the respective t_{depl} and μ_{molgas} means $\pm 1 \sigma$ dispersion of the ALPINE [C II]-detected non-merger galaxies in redshift bins of $4.4 < z < 4.6$ and $5.1 < z < 5.9$. The grey boxes represent the CO-detected galaxies from our compilation in redshift bins of $1 < z < 1.5$, $1.5 < z < 2.5$, and $2.5 < z < 3.7$, and the blue boxes the A³COSMOS galaxies at $0 < z < 1$ in $\Delta z = 0.3$ bins. The number drawn below boxes gives the number of galaxies used to derive the mean and 1σ dispersion. For comparison, we show with violet dotted, orange solid, and green dashed lines the multi-functional t_{depl} and μ_{molgas} best-fit functions of, respectively, Scoville et al. (2017), Liu et al. (2019b), and Tacconi et al. (2018), calculated for $\Delta MS = 0$ dex (the shaded areas define the $\Delta MS = \pm 0.3$ dex range) and for fixed stellar masses of $\log(M_{\text{stars}}/M_{\odot}) = 9.2$ (*left panels*) and $\log(M_{\text{stars}}/M_{\odot}) = 10$ (*right panels*).

as predicted by the three t_{depl} best-fit functions for MS galaxies with ΔMS ranging from -0.3 dex to $+0.3$ dex and stellar masses in two bins of $\log(M_{\text{stars}}/M_{\odot}) = 9.2_{-0.8}^{+0.3}$ and $\log(M_{\text{stars}}/M_{\odot}) = 10_{-0.5}^{+0.5}$. To compare the observations with the plotted best-fit functions, we bin the ALPINE galaxies in two redshift intervals of $4.4 < z < 4.6$ and $5.1 < z < 5.9$ (red boxes), and the CO-detected MS SFGs from our compilation (Sect. 4) in three redshift intervals of $1 < z < 1.5$, $1.5 < z < 2.5$, and $2.5 < z < 3.7$ (grey boxes). The blue boxes represent MS SFGs at $0 < z < 1$ from A³COSMOS in $\Delta z = 0.3$ bins (Liu et al. 2019b). The ALPINE galaxies exclude the t_{depl} best-fit function of Liu et al. (2019b) at $z \gtrsim 4.5$ in the two M_{stars} bins, but already in the redshift bin of $2.5 < z < 3.7$ we observe a deviation from this func-

tion in the $\log(M_{\text{stars}}/M_{\odot}) = 10_{-0.5}^{+0.5}$ bin. On the other hand, both the Scoville et al. (2017) and Tacconi et al. (2018) t_{depl} functions agree with the ALPINE observations, and this even if we consider the possible SFR_{IR} contribution for the ALPINE galaxies undetected in the FIR dust continuum (see Sect. 2), which would lower the plotted t_{depl} means by a factor of 1.5 in the redshift bin of $4.4 < z < 4.6$ and less in the higher redshift bin. The discrepancy of the Liu et al. (2019b) best-fit function with the other two functions results from the strong anti-correlation they find between t_{depl} and M_{stars} . This dependence of t_{depl} on M_{stars} is too strong for SFGs with $M_{\text{stars}} < 10^{10.5} M_{\odot}$ at $z \gtrsim 3$, but seems to be correct at the high M_{stars} end of $M_{\text{stars}} \gtrsim 10^{11} M_{\odot}$ where both the Scoville et al. (2017) and Tacconi et al. (2018) functions overes-

timate the t_{depl} measurements at $z \gtrsim 3$ (see Fig. 12 in Liu et al. 2019b). We postpone the refitting of the functional form of t_{depl} by including ALPINE galaxies in order to determine the scaling relation of t_{depl} over a more complete M_{stars} and redshift range to a future paper.

5.2. Molecular gas fraction

In Fig. 8 (top panel) we show the molecular gas fraction, defined as $f_{\text{molgas}} = M_{\text{molgas}} / (M_{\text{molgas}} + M_{\text{stars}})$, as a function of redshift for the ALPINE [C II]-detected non-merger galaxies (red circles) and [C II]-non-detected galaxies (light-red arrows) in the redshift bins of $4.4 < z < 4.6$ and $5.1 < z < 5.9$, and for our compilation of CO-detected MS SFGs from the literature separated in the same 6 redshift bins as in Sect. 5.1 and Fig. 6 of $z = 0$, $0 < z < 0.1$, $0.1 < z < 1$, $1 < z < 1.5$, $1.5 < z < 2.5$, and $2.5 < z < 3.7$, chosen in the way that the three bins between $z = 0.1$ and $z = 2.5$ contain a comparable number of galaxies (about 40). We then compute the respective means, errors on the mean, and standard deviations per redshift bin (black/grey big crosses). We show the ALPINE means obtained for the 44 [C II] detections (see Table 1). We also overplot the Béthermin et al. (2015) FIR SED stacks (light-grey shaded area). We observe a steep rise of f_{molgas} from $z = 0$ to $z \sim 3.7$, in agreement with what has been previously reported (e.g., Dessauges-Zavadsky et al. 2017; Scoville et al. 2017; Tacconi et al. 2018, 2020). With the ALPINE sample we probe, for the first time, the f_{molgas} evolution beyond $z \gtrsim 4.5$ in MS SFGs with a low median M_{stars} of $10^{9.7} M_{\odot}$. Within the 1σ dispersion on the f_{molgas} means in the two redshift bins, we observe a flattening of f_{molgas} that reaches a mean value of $63\% \pm 3\%$ over $z = 4.4 - 5.9$ (Table 1). The observed flattening is not subject to the assumptions that are needed to translate [C II] luminosities into molecular gas masses, since both $4.4 < z < 4.6$ and $5.1 < z < 5.9$ redshift bins are subject to those assumptions in the same way. When applying the survival analysis to take into account the ‘‘secure’’ 3σ upper limits of the ALPINE galaxies undetected in [C II] (Sect. 5.1), the f_{molgas} means in the $4.4 < z < 4.6$ and $5.1 < z < 5.9$ redshift bins drop to $46\% \pm 5\%$ (Table 1). This strengthens the f_{molgas} flattening toward high redshifts, which is an important result, consistent with the evolutionary trend of a constant sSFR beyond $z \gtrsim 4$ obtained by several studies (e.g., Tasca et al. 2015; Khusanova et al. 2020a), including the sSFR derived from the obscured SFR measured in the ALPINE galaxies by stacking the FIR dust continuum maps in the redshift bins of $4.4 < z < 4.6$ and $5.1 < z < 5.9$ (Khusanova et al. 2020b). The finding that f_{molgas} and sSFR merely have a similar evolution with redshift is not a surprise, since f_{molgas} can be expressed as a function of t_{depl} and sSFR (Tacconi et al. 2013):

$$f_{\text{molgas}} = \frac{1}{1 + (\text{sSFR } t_{\text{depl}})^{-1}}. \quad (7)$$

As a result, the f_{molgas} redshift evolution depends on the redshift evolution of both t_{depl} and sSFR. In the case of, on average, a weak change in t_{depl} of MS SFGs with redshift, which is what we observe in Fig. 6 (left panel), we globally have $f_{\text{molgas}}(z) \propto \text{sSFR}(z)$.

In the framework of the bathtub model, the f_{molgas} evolution with redshift reflects an interplay between cosmic inflow (supply of fresh gas onto galaxies) and gas consumption rates, modulo outflows. The mass accretion rate was shown to scale as $(1+z)^{2.25}$ (Dekel et al. 2009), therefore the gas supply rate drops faster with time than the gas consumption rate (see Sect. 5.1).

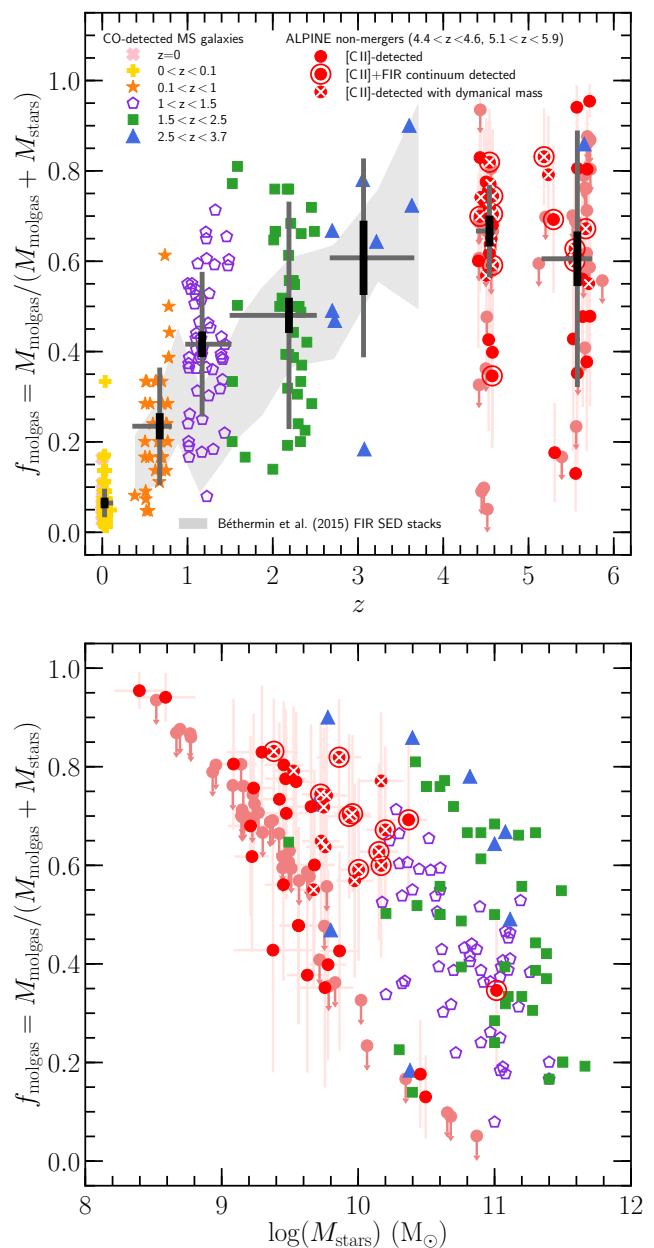


Fig. 8. Molecular gas fractions plotted for the same ALPINE galaxies (red circles) and CO-detected MS SFGs, with the same color-coding per redshift bin, as in Fig. 6. *Top panel.* Molecular gas fractions shown as a function of redshift. The respective means, errors on the mean, and standard deviations per redshift bin are indicated by the black/grey big crosses. The light-grey shaded area corresponds to the molecular gas fractions obtained by Béthermin et al. (2015) from FIR SED stacks. The f_{molgas} means per redshift bin show a steep increase from $z = 0$ to $z \sim 3.7$, followed by a flattening toward higher redshifts within the 1σ dispersion on the means. *Bottom panel.* Molecular gas fractions, restricted to $z \sim 1 - 5.9$ SFGs, shown as a function of stellar mass. A strong dependence of f_{molgas} on M_{stars} is observed for CO-detected high-redshift galaxies and the ALPINE galaxies as well.

This explains why galaxies at sufficiently high redshifts begin to be gas-rich, but then f_{molgas} drops as the gas consumption rate catches up. The phase during which galaxies have an excess of gas, and hence are in non-equilibrium, will also depend on feedback, since outflows, by ejecting the gas out of galaxies, reduce the amount of gas that needs to be processed into stars and help to establish the equilibrium earlier on. A quick look at the f_{molgas}

observations supports a gas excess until at most $z \sim 3$ (Fig. 8, top panel). This is much shorter in cosmic time than predicted by cosmological simulations of Lagos et al. (2015), who report a drop of f_{molgas} only several Gyr later, by $z \sim 1$. Given the shallow t_{depl} evolution with redshift, outflows must play an important role in blowing out part of the infalling gas at $z \gtrsim 3$. This is supported by signatures of star formation-driven outflows in stacks of [C II] spectra and [C II] moment-zero maps and stacks of rest-frame UV spectra of the ALPINE higher SFR ($\gtrsim 25 M_{\odot} \text{ yr}^{-1}$) galaxies (Ginolfi et al. 2020a; Faisst et al. 2020), but also observed in a few individual ALPINE objects with [C II] halos (Fujimoto et al. 2020; Ginolfi et al. 2020b). Observational evidence of star formation-driven outflows in SFGs at $z \lesssim 5 - 6$ was also reported in other studies (e.g., Sugahara et al. 2019; Rubin et al. 2014; Talia et al. 2017).

While we observe an overall flattening of f_{molgas} toward high redshifts, some individual galaxies appear to depart from this average trend considerably: the scatter in f_{molgas} among ALPINE MS SFGs ranges from $\sim 15\%$ to $\sim 95\%$. A significant scatter among f_{molgas} measurements is observed in all redshift bins (although the scatter is particularly large at $5.1 < z < 5.9$). The tight correlation between f_{molgas} and offset from the MS, reported even for MS SFGs lying within the ± 0.3 dex dispersion of the MS (Tacconi et al. 2013; Dessauges-Zavadsky et al. 2015; Genzel et al. 2015; Saintonge et al. 2016), certainly contributes to this f_{molgas} scatter per redshift bin. In addition to that, there is a strong dependence of f_{molgas} on M_{stars} as shown in the bottom panel of Fig. 8, previously found for local and $z \lesssim 3$ MS SFGs (e.g., Saintonge et al. 2011; Tacconi et al. 2013, 2018, 2020; Dessauges-Zavadsky et al. 2015; Schinnerer et al. 2016; Scoville et al. 2017), and now assessed for the ALPINE $z = 4.4 - 5.9$ galaxies (Spearman rank coefficient of -0.50 and p -value of 7.0×10^{-4}). The observed steep drop in f_{molgas} with increasing M_{stars} is expected from the gas conversion into stars, and is predicted by semi-analytical simulations developed in the framework of the bathtub model, as well as cosmological hydrodynamic simulations, for both local and high-redshift galaxies (Bouché et al. 2010; Davé et al. 2011, 2017). This behaviour was proposed to be consistent with the “downsizing” scenario, where at fixed redshift massive galaxies have lower f_{molgas} because they consumed their fuel of star formation earlier than less massive galaxies that still have large fractions of gas (Bouché et al. 2010; Santini et al. 2014; Dessauges-Zavadsky et al. 2015; Scoville et al. 2017). We find that the significant f_{molgas} scatter of ALPINE galaxies must be mostly driven by the large range of M_{stars} , from $10^{8.4} M_{\odot}$ to $10^{11} M_{\odot}$, they encompass.

Similarly to the multi-functional fitting performed by Scoville et al. (2017), Tacconi et al. (2018), and Liu et al. (2019b) for t_{depl} , we show in the bottom panels of Fig. 7 the best-fit functions obtained for the molecular gas ratio, $\mu_{\text{molgas}} = M_{\text{molgas}}/M_{\text{stars}}$, as a function of redshift for MS galaxies with ΔMS ranging from -0.3 dex to $+0.3$ dex and stellar masses in two bins of $\log(M_{\text{stars}}/M_{\odot}) = 9.2^{+0.3}_{-0.8}$ and $\log(M_{\text{stars}}/M_{\odot}) = 10^{+0.5}_{-0.5}$. We consider these two M_{stars} bins, because it is at these M_{stars} that the larger differences between the three fitted μ_{molgas} functions are found. To compare the observations with the plotted best-fit functions, we bin again the ALPINE galaxies in two redshift intervals of $4.4 < z < 4.6$ and $5.1 < z < 5.9$ (red boxes), and the CO-detected MS SFGs from our compilation (Sect. 4) in three redshift intervals of $1 < z < 1.5$, $1.5 < z < 2.5$, and $2.5 < z < 3.7$ (grey boxes). The blue boxes represent MS SFGs at $0 < z < 1$ from A³COSMOS in $\Delta z = 0.3$ bins (Liu et al. 2019b). Our data favour the Tacconi et al. (2018) best-fit function, given the comparable decrease of the predicted and measured μ_{molgas} at

Table 2. Stellar mass histories from multi-epoch abundance matching predictions of Behroozi et al. (2019)

$\langle z \rangle$	$M_{\text{halo}} = 10^{13} M_{\odot}$ at $z = 0$	$M_{\text{halo}} = 10^{14} M_{\odot}$ at $z = 0$
	M_{stars} range (M_{\odot})	M_{stars} range (M_{\odot})
0	$(5.9 - 16) \times 10^{10}$	$(2.5 - 5.0) \times 10^{11}$
0.7	$(3.4 - 12) \times 10^{10}$	$(1.2 - 2.7) \times 10^{11}$
1.2	$(2.2 - 10) \times 10^{10}$	$(1.0 - 1.8) \times 10^{11}$
2.2	$(3.0 - 43) \times 10^9$	$(4.3 - 10) \times 10^{10}$
3.0	$(8.0 - 180) \times 10^8$	$(1.8 - 8.0) \times 10^{10}$
4.5	$(1.0 - 29) \times 10^8$	$(2.9 - 27) \times 10^9$
5.5	$(3.2 - 130) \times 10^7$	$(1.3 - 8.0) \times 10^9$

$z = 4.4 - 5.9$, and the t_{depl} results discussed in Sect. 5.1. This function also provides a good fit to the μ_{molgas} redshift evolution of massive MS SFGs (see Fig. 13 in Liu et al. 2019b). On the other hand, the Scoville et al. (2017) function overestimates the molecular gas ratios of MS SFGs in both M_{stars} bins considered.

5.3. Molecular gas fraction over cosmic time

As stressed by Wiklind et al. (2019), to probe the true evolution of galaxy properties over cosmic time, galaxies need to be carefully selected in a way which correctly connects the progenitors at high redshifts with their descendants at $z = 0$. A possible selection method is to use the multi-epoch abundance matching, which links as a function of redshift the growth of central dark matter halos, as derived from numerical simulations, with the growth of stellar content constrained from observations of the M_{stars} function (Behroozi et al. 2013, 2019; Moster et al. 2013, 2018). The redshift evolution of the resulting stellar-to-halo mass relation is driven by gas accretion, star formation, feedback (leading to stellar mass loss), and eventually merging processes.

Following the work by Behroozi et al. (2019, top right panel of Fig. 18), we use the evolutionary corridors they computed, in the M_{stars} versus redshift plane, for the stellar mass histories of progenitors of $z = 0$ galaxies with a given M_{stars} range. The ALPINE [C II]-detected non-merger galaxies with their M_{stars} appear to be the progenitors, at $z \sim 4.5$ and $z \sim 5.5$, of Milky Way-like galaxies at $z = 0$ with M_{stars} in the range of $\sim 10^{10.8} M_{\odot}$ and $10^{11.2} M_{\odot}$ and of more massive $z = 0$ galaxies with $M_{\text{stars}} \sim 10^{11.4} - 10^{11.7} M_{\odot}$. The range of M_{stars} of these $z = 0$ descendants with halo masses of $M_{\text{halo}} = 10^{13} M_{\odot}$ and $10^{14} M_{\odot}$ at $z = 0$, respectively, were carefully chosen such that their respective stellar mass histories do not overlap in the $M_{\text{stars}} - z$ plane. In Table 2 we list the respective stellar mass histories. We then select, in our compilation of CO-detected MS SFGs and ALPINE galaxies, progenitors with the specific M_{stars} over cosmic time from $z > 0$ to $z = 5.9$.

As shown in Fig. 9, we find a different evolution of the molecular gas fraction from $z = 5.9$ to the present day for progenitors of Milky Way-analogues and for more massive $z = 0$ galaxies. Progenitors of Milky Way-like galaxies follow a monotonic decrease of f_{molgas} with cosmic time, which steepens at $z \lesssim 1$. However, this result relies on only three ALPINE f_{molgas} measurements in the redshift bin of $5.1 < z < 5.9$, which show galaxies dominated by gas with a mean f_{molgas} as high as $90\% \pm 4\%$. A larger sample of low M_{stars} galaxies in this redshift bin is necessary to confirm the currently observed monotonic decrease. Progenitors of the more massive $z = 0$ galaxies show, on the other hand, a steep f_{molgas} decline at $z \lesssim 2$, which is preceded

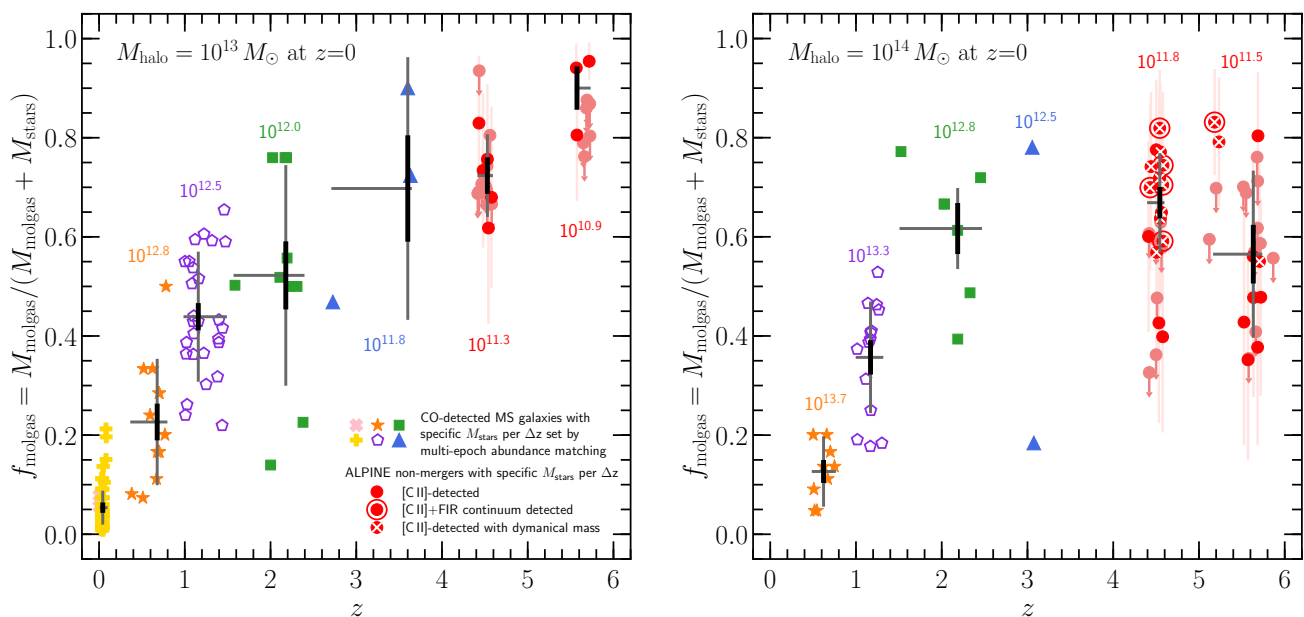


Fig. 9. Evolution of the molecular gas fraction with redshift plotted for the same ALPINE galaxies (red circles) and CO-detected MS SFGs, with the same color-coding per redshift bin, as in Fig. 6, but restricted to the $z > 0 - 5.9$ progenitors of the Milky Way-like galaxies at $z = 0$ with stellar masses in the range of $\sim 10^{10.8} - 10^{11.2} M_{\odot}$ for a halo mass of $10^{13} M_{\odot}$ (left panel), and more massive $z = 0$ galaxies with $M_{\text{stars}} \sim 10^{11.4} - 10^{11.7} M_{\odot}$ for a halo mass of $10^{14} M_{\odot}$ (right panel). We consider the progenitors' M_{stars} as a function of redshift listed in Table 2, obtained from the multi-epoch abundance matching predictions of Behroozi et al. (2019). The number drawn in each redshift bin corresponds to M_{halo} at this epoch. A different molecular gas fraction evolution from $z = 5.9$ to $z = 0$ is observed for the respective progenitors of the $10^{13} M_{\odot}$ and $10^{14} M_{\odot}$ halo mass galaxies at $z = 0$.

by a flat f_{molgas} evolution at higher redshifts, with a mean value of $63\% \pm 3\%$ at $z = 4.4 - 5.9$, although some hint of an f_{molgas} rise from $z \sim 5.5$ to $z \sim 4.5$ exits. How can we explain these different f_{molgas} evolutions with cosmic time?

As discussed in Sect. 5.2, galaxies are believed to be supplied with cold gas by cosmic accretion flows. This accreted gas can then be used for the M_{stars} build-up of galaxies, if not partly expelled by outflows from the galaxy. Ginolfi et al. (2020a) showed evidence of star formation-driven outflows in the [C II] emission stacks of the ALPINE galaxies with SFR higher than the median SFR of the ALPINE sample ($\text{SFR} > 25 M_{\odot} \text{ yr}^{-1}$). These higher SFR galaxies are also the more massive ones, due to their placement on the MS (Faisst et al. 2020). As a result, the observed outflows could contribute more to moderate the gas content available for star formation in the massive ALPINE galaxies, progenitors of $10^{14} M_{\odot}$ halo mass galaxies at $z = 0$, and could explain their flat f_{molgas} evolution from $z = 5.9$ to $z = 4.4$ (Fig. 9, right panel) given also the induced quenching of star formation yielding a temporarily decrease of the gas consumption rate. This scenario matches with the non-detection of star formation-driven outflows in the less star-forming (and therefore, on average, less massive) ALPINE galaxies (Ginolfi et al. 2020a), progenitors at $z = 4.4 - 5.9$ of Milky Way-like galaxies, and hence with the observed steady decrease of their f_{molgas} from $z = 5.9$ to $z = 4.4$ (Fig. 9, left panel).

Moreover, it has also been suggested by simulations that for very massive dark matter halos the gas supply starts to shut off and prevents star formation (Dekel & Birnboim 2006; Kereš et al. 2009; Bouché et al. 2010). This is due to the fact that as the halo grows larger, it reaches the threshold for virial shock heating ($M_{\text{shock}} \lesssim 10^{12} M_{\odot}$) and, consequently, the infalling cold gas shock heats up close to the virial temperature (Dekel et al. 2009). Our data suggest that this might be happening at $z \sim 5$ in $\sim 10^{11.5-11.8} M_{\odot}$ halos, the progenitors of $z = 0$ halos of $10^{14} M_{\odot}$

(see Fig. 9, right panel). This indirectly implies that these massive galaxies must be mature by $z \sim 5$ and probably quench earlier than lower mass galaxies. Comparing right and left panels of Fig. 9, we observe that the f_{molgas} means of massive galaxies are smaller by $\sim 10\%$ (on absolute scale) in the redshift bins of $1 < z < 1.5$ and $0.1 < z < 1$ than those of lower mass galaxies.

On the other hand, massive progenitors have to grow a lot in the past to build up their large M_{stars} . But, is there still enough cold gas for them to grow sufficiently quickly to reach these M_{stars} by $z \sim 5$, if we advocate that the cold gas accreted on galaxies is either removed by outflows or reduced because of the suppression of the cosmic accretion flows? The constant f_{molgas} observed between $z = 5.9$ and $z = 4.4$, with even a possibly lower f_{molgas} value in the $5.1 < z < 5.9$ redshift bin, may also be the result of an efficient star formation in these massive SFGs, such that the infalling gas is rapidly converted into stars. Some evidence for a higher SFE in massive ALPINE galaxies is shown in Fig. 6 (right panel), where, when considering the ALPINE galaxies only, we see a trend for an anti-correlation between t_{depl} and M_{stars} (Spearman rank coefficient of -0.33 and p -value of 0.0016). Liu et al. (2019b) reported such an anti-correlation, but for the whole sample of SFGs from $z \sim 6$ to $z = 0$. We find, on the contrary, that this anti-correlation is not present for MS SFGs at $z \lesssim 3.7$ (see also Dessauges-Zavadsky et al. 2015; Tacconi et al. 2018). We rather argue that the t_{depl} dependence on M_{stars} might change across the cosmic time, from a negative slope at high redshift to the positive slope that is observed for local galaxies (e.g., Saintonge et al. 2017).

6. Summary and conclusions

We use observations from the ALPINE [C II] $158 \mu\text{m}$ survey of UV-selected star-forming galaxies at $z = 4.4 - 5.9$ (Le Fèvre et al. 2020; Faisst et al. 2020; Béthermin et al. 2020) and the

correlation between [C II] luminosity and molecular gas mass recently proposed by Zanella et al. (2018), to obtain $M_{\text{molgas}}^{\text{CII}}$ estimates of 44 [C II]-detected MS SFGs with a median M_{stars} of $10^{9.7} M_{\odot}$ (Fig. 1). Prior our work, measurements of M_{molgas} at $z > 4$ have been derived for 24 MS SFGs from A³COSMOS based on the thermal dust FIR continuum emission (Liu et al. 2019b), all having M_{stars} one order of magnitude larger than those of ALPINE galaxies. And only two CO-derived molecular gas masses have been reported in MS SFGs at $z > 5$ (Pavesi et al. 2019; D’Odorico et al. 2018).

The [C II] luminosity appears to be an effective tracer of the gas mass of ALPINE galaxies with a 1σ uncertainty of 0.3 dex. This level of error is assessed by comparing molecular gas mass estimates based on [C II] luminosity, rest-frame $158 \mu\text{m}$ continuum emission (measured for 11 galaxies; Fig. 3), and dynamical mass (determined for 17 galaxies with size measurements; Fig. 4). The agreement with the dynamical mass, essentially probing the baryonic gas mass after removing M_{stars} (the relative dark matter contribution in the internal regions of galaxies is expected to be low), supports that L_{CII} likely traces the total gas mass including the molecular, atomic, and ionised gas phases, and hence possibly overestimates the true M_{molgas} unless the atomic and ionised gas masses are negligible as often assumed at high redshift.

Accurate M_{stars} and SFR were obtained for the ALPINE galaxies from existing ancillary UV to IR data (Faisst et al. 2020). Together with M_{molgas} , we derive fundamental physical quantities, which are the molecular gas depletion timescale and the molecular gas fraction, and explore scaling-relations between these physical quantities. To put the ALPINE galaxies in a global context, we build a comparison sample of MS SFGs between $z = 0$ and $z \sim 3.7$ with molecular gas mass measurements inferred from CO luminosities reported in the literature. Our main results can be summarized as follows:

- The ALPINE sample enables us to explore the t_{depl} evolution beyond $z \gtrsim 4.5$ for a statistically significant number of MS SFGs. We observe a continuous decline of t_{depl} from $z = 0$ to $z \sim 5.9$, reaching a mean value of $(4.6 \pm 0.8) \times 10^8$ yr at $z = 5.1 - 5.9$, which confirms a t_{depl} redshift evolution with a slope shallower than $(1 + z)^{-1.5}$ that is predicted in the framework of the bathtub model (Fig. 6, left panel). This suggests that MS SFGs at $z \gtrsim 4.5$ are not considerably more efficient in forming stars, only a factor of 2 – 3 with respect to present-day galaxies, or undergo a significant increase in their f_{molgas} . The large t_{depl} scatter of more than 1 dex per redshift bin is attributed to the multi-functional dependence of t_{depl} on various physical parameters, such as their offset from the MS, star formation rate, and stellar mass. With the ALPINE galaxies probing low-to-moderate M_{stars} with a median of $10^{9.7} M_{\odot}$, we find that MS SFGs at $z \sim 1 - 5.9$ show no t_{depl} dependence on M_{stars} (Fig. 6, right panel).
- We confirm that the steep rise of f_{molgas} is confined between $z = 0$ and $z \sim 3.7$. At higher redshift, as shown by ALPINE galaxies, the f_{molgas} evolution flattens and reaches a mean value as high as $63\% \pm 3\%$ over $z = 4.4 - 5.9$ (Fig. 8, top panel). The f_{molgas} flattening is consistent with the sSFR redshift evolution, which also flattens beyond $z \gtrsim 4$ according to several studies, including the results on the obscured SFR measured in the ALPINE galaxies by stacking the FIR dust continuum maps (Khusanova et al. 2020b). The redshift, at which the turnover in the f_{molgas} evolution happens, depends on when the gas consumption rate catches up to the mass accretion rate. We observe a gas excess until at most $z \sim 3$,

which, given the slow t_{depl} evolution with redshift, suggests that outflows may play an important role in blowing out part of the infalling gas at $z \gtrsim 4$. We attribute the large scatter in f_{molgas} of ALPINE galaxies, from $\sim 10\%$ to $\sim 95\%$, to mostly M_{stars} (Fig. 8, lower panel), given the strong dependence of f_{molgas} observed on M_{stars} (Fig. 8, bottom panel) that reflects an important “downsizing” effect from massive to low-mass galaxies at $z = 4.4 - 5.9$.

- The [C II]-detected ALPINE galaxies at $z = 4.4 - 5.9$ and the currently available compilation of f_{molgas} measurements in CO-detected MS SFGs at $z \sim 0 - 3.7$ enables us, for the first time, to probe the f_{molgas} evolution over cosmic time, from $z = 5.9$ to the present day, of the progenitors of $z = 0$ Milky Way-like galaxies with M_{stars} in the range of $\sim 10^{10.8} - 10^{11.2} M_{\odot}$ for a halo mass of $10^{13} M_{\odot}$ and of more massive $z = 0$ galaxies with $M_{\text{stars}} \sim 10^{11.4} - 10^{11.7} M_{\odot}$ for a halo mass of $10^{14} M_{\odot}$. We use the multi-epoch abundance matching predictions of Behroozi et al. (2019) to select progenitors’ M_{stars} as a function of redshift (Table 2). We observe a different redshift evolution of f_{molgas} for the respective progenitors of galaxy halos of different masses (Fig. 9), where lower mass halos ($M_{\text{halo}} = 10^{13} M_{\odot}$ at $z = 0$) show a monotonic decrease of f_{molgas} with cosmic time and the higher mass halos ($M_{\text{halo}} = 10^{14} M_{\odot}$ at $z = 0$) show, on average, a flat f_{molgas} until $z \sim 2$ followed by a steep decrease at $z \lesssim 2$. This difference, if confirmed, likely reveals important changes in the physical conditions of MS SFGs at $z \sim 5$ for a specific halo mass threshold. To explain the flat f_{molgas} evolution from $z = 5.9$ to $z = 4.4$ of progenitors of $z = 0$ halos with $10^{14} M_{\odot}$ masses, we discuss the effect of possibly stronger star formation-driven outflows in these more massive ALPINE galaxies as observed by Ginolfi et al. (2020a, and also Fujimoto et al. 2020, Faisst et al. 2020), which could remove their accreted cold gas and temporarily quench star formation. Simulations also suggest that for very massive dark matter halos, the gas supply starts to shut off. According to the f_{molgas} redshift evolution observed for the ALPINE galaxies, this seems to happen at $z \sim 5$ in halos of $\sim 10^{11.5-11.8} M_{\odot}$, progenitors of $10^{14} M_{\odot}$ halos at $z = 0$. Alternatively, we argue for a possible evidence of a higher SFE in the more massive ALPINE galaxies that is also necessary for the quick stellar mass build-up of these galaxies. To conclude, certainly the three effects, namely outflows, halt of gas supplying, and over-efficient star formation, jointly contribute to the f_{molgas} plateau observed for the massive galaxies at $z = 4.4 - 5.9$.

Acknowledgements. This paper is based on data obtained with the ALMA Observatory, under Large Program 2017.1.00428.L. ALMA is a partnership of ESO (representing its member states), NSF(USA) and NINS (Japan), together with NRC (Canada), MOST and ASIAA (Taiwan), and KASI (Republic of Korea), in cooperation with the Republic of Chile. The Joint ALMA Observatory is operated by ESO, AUI/NRAO and NAOJ. This program receives financial support from the French CNRS-INSU Programme National Cosmologie et Galaxies. F.P., F.L., A.C., C.G., and M.T. acknowledge the support from grant PRIN MIUR 2017 - 20173ML3WW_001. S.F. is supported by the Cosmic Dawn Center of Excellence funded by the Danish National Research Foundation under the grant No. 140. J.D.S. is supported by the JSPS KAKENHI Grant Number JP18H04346, and the World Premier International Research Center Initiative (WPI Initiative), MEXT, Japan. G.C.J. acknowledges ERC Advanced Grant 695671 “QUENCH” and support by the Science and Technology Facilities Council (STFC). M.B. acknowledges FONDECYT regular grant 1170618. E.I. acknowledges partial support from FONDECYT through grant No. 1171710. S.T. acknowledges support from the European Research Council (ERC) Consolidator Grant funding scheme (project “ConText”, grant number: 648179). The Cosmic Dawn Center (DAWN) is funded by the Danish National Research Foundation under grant No. 140. L.V. acknowledges funding from the European Union’s Horizon 2020 research

and innovation program under the Marie Skłodowska-Curie Grant agreement No. 746119.

References

- Accurso, G., Saintonge, A., Bisbas, T. G., & Viti, S. 2017, *MNRAS*, 464, 3315
- Aravena, M., Decarli, R., González-López, J., et al. 2019, *ApJ*, 882, 136
- Asplund, M., Grevesse, N., Sauval, A. J., Allende Prieto, C., & Kiselman, D. 2004, *A&A*, 417, 751
- Barnabè, M., Dutton, A. A., Marshall, P. J., et al. 2012, *MNRAS*, 423, 1073
- Behroozi, P. S., Wechsler, R. H., & Conroy, C. 2013, *ApJ*, 770, 57
- Behroozi, P. S., Wechsler, R. H., Hearin, A. P., & Conroy, C. 2019, *MNRAS*, 488, 3143
- Béthermin, M., Daddi, E., Magdis, G., et al. 2015, *A&A*, 573, A113
- Béthermin, M., Wu, H.-Y., Lagache, G., et al. 2017, *A&A*, 607, A89
- Béthermin, M., Fudamoto, Y., Ginolfi, M., et al. 2020, *A&A*, submitted [arXiv:2002.00962]
- Bigiel, F., Leroy, A., Walter, F., et al. 2008, *AJ*, 136, 2846
- Bolatto, A. D., Wolfire, M., & Leroy, A. K. 2013, *ARA&A*, 51, 207
- Bouché, N., Dekel, A., Genzel, R., et al. 2010, *ApJ*, 718, 1001
- Bourne, N., Dunlop, J. S., Simpson, J. M., Rowlands, K. E., Geach, J. E., & McLeod, D. J. 2019, *MNRAS*, 482, 3135
- Bothwell, M. S., Smail, I., Chapman, S. C., et al. 2013, *MNRAS*, 429, 3047
- Casey, C. M., Chen, C.-C., Cowie, L. L., et al. 2013, *MNRAS*, 436, 1919
- Cassata, P., Liu, D., Groves, B., et al. 2020, *ApJ*, in press [arXiv:2002.04040]
- Capak, P. L., Carilli, C., Jones, G., et al. 2015, *Nature*, 522, 455
- Carilli, C. L., & Walter, F. 2013, *ARA&A*, 51, 105
- Chabrier, G. 2003, *PASP*, 115, 763
- Cormier, D., Madden, S. C., Leboutteiller, V., et al. 2015, *A&A*, 578, A53
- Daddi, E., Bournaud, F., Walter, F., et al. 2010, *ApJ*, 713, 686
- Daddi, E., Dannerbauer, H., Liu, D., et al. 2015, *A&A*, 577, A46
- Davé, R., Finlator, K., & Oppenheimer, B. 2011, *MNRAS*, 416, 1354
- Davé, R., Finlator, K., & Oppenheimer, B. 2012, *MNRAS*, 421, 98
- Davé, R., Rafieferantsoa, M. H., Thompson, R. J., & Hopkins, P. F. 2017, *MNRAS*, 467, 115
- Davidzon, I., Ilbert, O., Laigle, C., et al. 2017, *A&A*, 605, A70
- Davidzon, I., Ilbert, O., Faisst, A. L., Sparre, M., & Capak, P. L. 2018, *ApJ*, 852, 107
- Decarli, R., Walter, F., González-López, J., et al. 2019, *ApJ*, 882, 138
- Dekel, A., & Birnboim, Y. 2006, *MNRAS*, 368, 2
- Dekel, A., Birnboim, Y., Engel, G., et al. 2009, *Nature*, 457, 451
- Dekel, A., & Mandelker, N. 2014, *MNRAS*, 444, 2071
- de Looze, I., Baes, M., Bendo, G. J., Cortese, L., & Fritz, J. 2011, *MNRAS*, 416, 2712
- de Looze, I., Cormier, D., Leboutteiller, V., et al. 2014, *A&A*, 568, A62
- Dessauges-Zavadsky, M., Zamojski, M., Schaerer, D., et al. 2015, *A&A*, 577, A50
- Dessauges-Zavadsky, M., Zamojski, M., Rujopakarn, W., et al. 2017, *A&A*, 605, A81
- Dessauges-Zavadsky, M., Richard, J., Combes, F., et al. 2019, *Nature As.*, 3, 1115
- Díaz-Santos, T., Armus, L., Charmandaris, V., et al. 2017, *ApJ*, 846, 32
- D’Odorico, V., Feruglio, C., Ferrara, A., et al. 2018, *ApJL*, 863, L29
- Erb, D. K., Steidel, C. C., Shapley, A. E., et al. 2006, *ApJ*, 644, 813
- Faisst, A. L., Capak, P., Hsieh, B. C., et al. 2016, *ApJ*, 821, 122
- Faisst, A. L., Schaerer, D., Lemaux, B. C., et al. 2020, *ApJS*, submitted [arXiv:1912.01621]
- Feldmann, R. 2015, *MNRAS*, 449, 3274
- Förster Schreiber, N. M., Genzel, R., Bouché, N., et al. 2009, *ApJ*, 706, 1364
- Freundlich, J., Combs, F., Tacconi, L. J., et al. 2019, *A&A*, 622, 105
- Fudamoto, Y., Oesch, P. A., Faisst, A., et al. 2020, *MNRAS*, submitted
- Fujimoto, S., Silverman, J. D., Béthermin, M., et al. 2020, *A&A*, submitted [arXiv:2003.00013]
- Genel, S., Vogelsberger, M., Springel, V., et al. 2014, *MNRAS*, 445, 175
- Genzel, R., Tacconi, L. J., Gracia-Carpio, J., et al. 2010, *MNRAS*, 407, 2091
- Genzel, R., Tacconi, L. J., Combes, F., et al. 2012, *ApJ*, 746, 69
- Genzel, R., Tacconi, L. J., Lutz, D., et al. 2015, *ApJ*, 800, 20
- Giacconi, R., Zirm, A., Wang, J., et al. 2002, *ApJS*, 139, 369
- Girard, M., Dessauges-Zavadsky, M., Schaerer, D., et al. 2018, *A&A*, 613, A72
- Ginolfi, M., Hunt, L. K., Tortora, C., Schneider, R., & Cresci, G. 2019, *A&A*, in press [arXiv:1907.06654]
- Ginolfi, M., Jones, G. C., Béthermin, M., et al. 2020a, *A&A*, 633, A90
- Ginolfi, M., Jones, G. C., Béthermin, M., et al. 2020b, *A&A*, submitted
- González-López, J., Barrientos, L. F., Gladders, M. D., et al. 2017, *ApJL*, 846, L22
- Gowardhan, A., Riechers, D., Pavesi, R., Daddi, E., Dannerbauer, H., & Neri, R. 2019, *ApJ*, 875, 6
- Groves, B. A., Schinnerer, E., Leroy, A., et al. 2015, *ApJ*, 799, 96
- Hughes, T. M., Ibar, E., Villanueva, V., et al. 2017a, *A&A*, 602, A49
- Hughes, T. M., Ibar, E., Villanueva, V., et al. 2017b, *MNRAS*, 468, 103
- Isobe, T., Feigelson, E. D., & Nelson, P. I. 1986, *ApJ*, 306, 490
- Jones, G. C., Béthermin, M., Fudamoto, Y., et al. 2020, *MNRAS*, 491, L18
- Kaasinen, M., Scoville, N. Z., Walter, F., et al. 2019, *ApJ*, 880, 15
- Kennicutt, R. C. Jr. 1998a, *ApJ*, 498, 541
- Kennicutt, Jr., R. C. 1998b, *ARA&A*, 36, 189
- Kereš, D., Katz, N., Weinberg, D. H., & Davé, R. 2005, *MNRAS*, 363, 2
- Kereš, D., Katz, N., Fardal, M., Davé, R., & Weinberg, D. H. 2009, *MNRAS*, 395, 160
- Khusanova, Y., Le Fèvre, O., Cassata, P., et al. 2020a, *A&A*, 634, A97
- Khusanova, Y., Béthermin, M., Le Fèvre, O., et al. 2020b, *A&A*, in prep.
- Lagos, C. del P., Crain, R. A., Schaye, J., et al. 2015, *MNRAS*, 452, 3815
- Law, D. R., Steidel, C. C., Erb, D. K., et al. 2009, *ApJ*, 697, 2057
- Lee, N., Sanders, D. B., Casey, C. M., et al. 2015, *ApJ*, 801, 80
- Le Fèvre, O., Béthermin, M., Faisst, A., et al. 2020, *A&A*, submitted [arXiv:1910.09517]
- Leroy, A. K., Bolatto, A., Gordon, K., et al. 2011, *ApJ*, 737, 12
- Leroy, A. K., Walter, F., Sandstrom, K., et al. 2013, *AJ*, 146, 19
- Li, Q., Narayanan, D., Davé, R., & Krumholz, M. R. 2018, *ApJ*, 869, 73
- Lilly, S. J., Carollo, C. M., Pipino, A., Renzini, A., & Peng, Y. 2013, *ApJ*, 772, 119
- Liu, D., Lang, P., Magnelli, B., et al. 2019a, *ApJS*, 244, 40
- Liu, D., Schinnerer, E., Groves, B., et al. 2019b, *ApJ*, 887, 235
- Madden, S. C., Geis, N., Genzel, R., et al. 1993, *ApJ*, 407, 579
- Magdis, G. E., Daddi, E., Elbaz, D., et al. 2011, *ApJ*, 740, 15
- Magdis, G. E., Daddi, E., Béthermin, M., et al. 2012, *ApJ*, 760, 6
- Magdis, G. E., Rigopoulou, D., Daddi, E., et al. 2017, *A&A*, 603, A93
- Magnelli, B., Saintonge, A., Lutz, D., et al. 2012, *A&A*, 548, A22
- Maiolino, R., Nagao, T., Grazian, A., et al. 2008, *A&A*, 488, 463
- Malhotra, S., Kaufman, M. J., Hollenbach, D., et al. 2001, *ApJ*, 561, 766
- Maloney, P., & Black, J. H. 1988, *ApJ*, 325, 389
- Mannucci, F., Cresci, G., Maiolino, R., et al. 2010, *MNRAS*, 408, 2115
- Martí-Vidal, I., Vlemmings, W. H. T., Muller, S., & Casey, S. 2014, *A&A*, 563, A136
- McMullin, J. P., Waters, B., Schiebel, D., Young, W., & Golap, K. 2007, in *Astronomical Society of the Pacific Conference Series*, Vol. 376, *Astronomical Data Analysis Software and Systems XVI*, ed. R. A. Shaw, F. Hill, & D. J. Bell, 127
- Molina, J., Ibar, E., Swinbank, A. M., et al. 2017, *MNRAS*, 466, 892
- Molina, J., Ibar, E., Smail, I., et al. 2019, *MNRAS*, 487, 4856
- Moster, B. P., Naab, T., & White, S. D. M. 2013, *MNRAS*, 428, 3121
- Moster, B. P., Naab, T., & White, S. D. M. 2018, *MNRAS*, 477, 1822
- Narayanan, D., & Krumholz, M. R. 2017, *MNRAS*, 467, 50
- Noble, A. G., McDonald, M., Muzzini, A., et al. 2017, *ApJL*, L21, 6
- Olsen, K., Greve, T. R., Narayanan, D., et al. 2018, *ApJ*, 857, 148
- Orr, M. E., Hayward, C. C., & Hopkins, P. F. 2019, *MNRAS*, 486, 4724
- Pallottini, A., Ferrara, A., Bovino, S., et al. 2017, *MNRAS*, 471, 4128
- Papovich, C., Labbé, I., Glazebrook, K., et al. 2016, *Nature As.*, 1, 3
- Pavesi, R., Riechers, D. A., Faisst, A. L., Stacey, G. J., & Capak, P. L. 2019, *ApJ*, 882, 168
- Pettini, M., & Pagel, B. E. J. 2004, *MNRAS*, 348, 59
- Pineda, J. L., Langer, W. D., & Goldsmith, P. F. 2014, *A&A*, 570, A121
- Priyon, G. C., Narayanan, D., & Davé, R. 2018, *ApJ*, 867, 102
- Ribeiro, B., Le Fèvre, O., Tasca, L. A. M., et al. 2016, *A&A*, 593, A22
- Rodighiero, G., Daddi, E., Baronchelli, I., et al. 2011, *ApJ*, 739, 40
- Rubin, K. H. R., Prochaska, J. X., Koo, D. C., et al. 2014, *ApJ*, 794, 156
- Sugahara, Y., Ouchi, M., Harikane, Y., Bouché, N., Mitchell, P. D., & Blaizot, J. 2019, *ApJ*, 886, 29
- Saintonge, A., Kauffmann, G., Wang, J., et al. 2011, *MNRAS*, 415, 61
- Saintonge, A., Lutz, D., Genzel, R., et al. 2013, *ApJ*, 778, 2
- Saintonge, A., Catinella, B., Cortese, L., et al. 2016, *MNRAS*, 462, 1749
- Saintonge, A., Catinella, B., Tacconi, L. J., et al. 2017, *ApJS*, 233, 22
- Santini, P., Maiolino, R., Magnelli, B., et al. 2014, *A&A*, 562, A30
- Sargent, M. T., Daddi, E., Béthermin, M., et al. 2014, *ApJ*, 793, 19
- Schaerer, D., Ginolfi, M., Le Fèvre, O., et al. 2020, *A&A*, submitted [arXiv:2002.00979]
- Schinnerer, E., Groves, B., Sargent, M. T., et al. 2016, *ApJ*, 833, 112
- chreiber, C., Elbaz, D., Pannella, M., et al. 2018, *A&A*, 609, A30
- Scoville, N., Aussel, H., Brusa, M., et al. 2007, *ApJS*, 172, 1
- Scoville, N., Aussel, H., Sheth, K., et al. 2014, *ApJ*, 783, 84
- Scoville, N., Sheth, K., Aussel, H., et al. 2016, *ApJ*, 820, 83
- Scoville, N., Lee, N., Vanden Bout, P., et al. 2017, *ApJ*, 837, 150
- Seko, A., Ohta, K., Yabe, K., et al. 2016, *ApJ*, 819, 82
- Silverman, J. D., Daddi, E., Rodighiero, G., et al. 2015, *ApJL*, 812, L23
- Silverman, J. D., Rujopakarn, W., Daddi, E., et al. 2018, *ApJ*, 867, 92
- Speagle, J. S., Steinhardt, C. L., Capak, P. L., & Silverman, J. D. 2014, *ApJS*, 214, 15
- Stacey, G. J., Geis, N., Genzel, R., et al. 1991, *ApJ*, 373, 423
- Strong, A. W., & Mattox, J. R. 1996, *A&A*, 308, L21

- Tacchella, S., Dekel, A., Carollo, C. M., et al. 2016, MNRAS, 457, 2790
 Tacconi, L. J., Neri, R., Genzel, R., et al. 2013, ApJ, 768, 74
 Tacconi, L. J., Genzel, R., Saintonge, A., et al. 2018, ApJ, 853, 179
 Tacconi, L. J., Genzel, R., & Sternberg, A. 2020, ARA&A, submitted [arXiv:2003.06245]
 Tadaki, K., Kodama, T., Hayashi, M., et al. 2019, PASJ, 71, 40
 Talia, M., Brusa, M., Cimatti, A., et al. 2017, MNRAS, 471, 4527
 Talia, M., et al. 2020, MNRAS, submitted
 Tasca, L. A. M., Le Fèvre, O., Hathi, N. P., et al. 2015, A&A, 581, A54
 Valentino, F., Magdis, G. E., Daddi, E., et al. 2018, ApJ, 869, 27
 Vallini, L., Gallerani, S., Ferrara, A., Pallottini, A., & Yue, B. 2015, ApJ, 813, 36
 Vallini, L., Pallottini, A., Ferrara, A., Gallerani, S., Sobacchi, E., & Behrens, C. 2018, MNRAS, 473, 271
 Wang, R., Wagg, J., Carilli, C. L., et al. 2013, ApJ, 773, 44
 Whitaker, K. E., Franx, M., Leja, J., et al. 2014, ApJ, 795, 104
 Wisnioski, E., Förster Schreiber, N. M., Wuyts, S., et al. 2015, ApJ, 799, 209
 Wiklind, T., Ferguson, H. C., Guo, Y., et al. 2019, ApJ, 878, 83
 Wolfire, M. G., Hollenbach, D., & McKee, C. F. 2010, ApJ, 716, 1191
 Wuyts, E., Kurk, J., Förster Schreiber, N. M., et al. 2014, ApJ, 789, 40
 Zahid, H. J., Kashino, D., Silverman, J. D., et al. 2014, ApJ, 792, 75
 Zanella, A., Daddi, E., Magdis, G., et al. 2018, MNRAS, 481, 1976

-
- ¹ Observatoire de Genève, Université de Genève, 51 Ch. des Maillettes, 1290 Versoix, Switzerland
 e-mail: miroslava.dessauges@unige.ch
- ² Università di Bologna - Dipartimento di Fisica e Astronomia, Via Gobetti 93/2 - 40129, Bologna, Italy
- ³ INAF - Osservatorio di Astrofisica e Scienza dello Spazio di Bologna, via Gobetti 93/3, 40129, Bologna, Italy
- ⁴ Aix Marseille Université, CNRS, LAM (Laboratoire d'Astrophysique de Marseille) UMR 7326, 13388, Marseille, France
- ⁵ The Cosmic Dawn Center, University of Copenhagen, Vibenshuset, Lyngbyvej 2, 2100 Copenhagen, Denmark
- ⁶ Niels Bohr Institute, University of Copenhagen, Lyngbyvej 2, 2100 Copenhagen, Denmark
- ⁷ Kavli Institute for the Physics and Mathematics of the Universe, The University of Tokyo, Kashiwa, Japan 277-8583 (Kavli IPMU, WPI)
- ⁸ Department of Astronomy, School of Science, The University of Tokyo, 7-3-1 Hongo, Bunkyo, Tokyo 113-0033, Japan
- ⁹ Cavendish Laboratory, University of Cambridge, 19 J. J. Thomson Ave., Cambridge CB3 0HE, UK
- ¹⁰ Kavli Institute for Cosmology, University of Cambridge, Madingley Road, Cambridge CB3 0HA, UK
- ¹¹ IPAC, M/C 314-6, California Institute of Technology, 1200 East California Boulevard, Pasadena, CA 91125, USA
- ¹² Max-Planck-Institut für Astronomie, Königstuhl 17, 69117 Heidelberg, Germany
- ¹³ Dipartimento di Fisica e Astronomia, Università di Padova, vicolo dell'Osservatorio, 3 35122 Padova, Italy
- ¹⁴ INAF - Osservatorio Astronomico di Padova, vicolo dell'Osservatorio 5, 35122 Padova, Italy
- ¹⁵ The Caltech Optical Observatories, California Institute of Technology, Pasadena, CA 91125, USA
- ¹⁶ Instituto de Investigación Multidisciplinar en Ciencia y Tecnología, Universidad de La Serena, Raúl Bitrán 1305, La Serena, Chile
- ¹⁷ Departamento de Astronomía, Universidad de La Serena, Av. Juan Cisternas 1200 Norte, La Serena, Chile
- ¹⁸ Centro de Astronomía (CITEVA), Universidad de Antofagasta, Avenida Angamos 601, Antofagasta, Chile
- ¹⁹ INAF - Osservatorio Astrofisico di Arcetri, Largo E. Fermi 5, 50125, Firenze, Italy
- ²⁰ Space Telescope Science Institute, 3700 San Martin Drive, Baltimore, MD 21218, USA
- ²¹ Instituto de Física y Astronomía, Universidad de Valparaíso, Avda. Gran Bretaña 1111, Valparaíso, Chile
- ²² Department of Physics, University of California, Davis, One Shields Ave., Davis, CA 95616, USA
- ²³ Department of Astronomy, University of Florida, 211 Bryant Space Sciences Center, Gainesville, FL 32611 USA
- ²⁴ Leiden Observatory, Leiden University, PO Box 9500, 2300 RA Leiden, The Netherlands